TECHNICKÁ UNIVERZITA V LIBERCI
Fakulta mechatroniky, informatiky
a mezioborových studií

SYNTÉZA A FUNKCIONALIZACE UHLÍKATÝCH NANOMATERIÁLŮ PRO TKÁŇOVÉ INŽENÝRSTVÍ

SYNTHESIS AND FUNCTIONALISATION OF CARBON NANOMATERIALS FOR TISSUE ENGINEERING

Autoreferát disertační práce

Studijní program:	P 3901 Aplikované vědy v inženýrství
Studijní obor:	3901V055 Aplikované vědy v inženýrství
Autor práce:	Mgr. Jana Karpíšková
Školitel:	Prof. Ing. Ivan Stibor, CSc.

ANNOTATION

Research of materials suitable for tissue engineering is a rapidly developing area. Among many other, various carbon materials have been successfully used for cell cultivation. There are a lot of factors that have been proved to affect cell adhesion and proliferation, such as the presence of various chemical groups, wettability of the surface, surface energy, morphology, mechanical properties etc.

In this work, a novel type of functionalisation was performed, in which carbon nanoparticles (CNPs) were successfully functionalised with amide-amine groups. The size and form of the CNPs was investigated by transmission electron microscopy (TEM). The specific surface areas and pore volumes of the particles were measured via N adsorption and calculated from Brunauer-Emmet-Teller (BET) equation. The chemical composition was studied via X-ray photoelectron spectroscopy (XPS) and organic elemental analysis (OEA). Differential scanning calorimetry (DSC) was used to investigate thermal stability of CNPs.

The functionalised CNPs were grafted onto the surface of polyethylene terephthalate (PET) and high density polyethylene (HDPE) pre-activated in argon plasma. The chemical composition of the modified polymer surfaces was determined by Raman and X-ray photoelectron spectroscopies and by electrokinetic analysis (zeta potential). Surface roughness and morphology of polymers grafted with CNPs was studied by atomic force microscopy (AFM), surface contact angle was measured by goniometry. Adhesion and proliferation of rat vascular smooth muscle cells (VSMC) on HDPE and PET surfaces grafted with functionalised CNPs were studied *in vitro*.

Using the aforementioned CNPs, four types of composite scaffolds were prepared via sputtering the CNPs into electrospun polycaprolactone (PCL) nanofibers: three of them with three types of functionalised CNPs and one with plain activated CNPs. Plain PCL nanofibers and the composite nanofibrous scaffold with plain activated CNPs were used as comparative samples. The structure of the materials was studied using scanning electron microscopy (SEM). The specific surface area of the scaffolds was measured via N and Kr adsorption and calculated from BET equation. Cell viability of 3T3 mouse fibroblasts and proliferation was measured by MTT assay on days 1, 3, 8 and 14. The samples were then stained using fluorescent dyes and examined via fluorescence microscopy (FM). During the FM analyses, all scaffolds containing CNPs underwent structural degradation when irradiated with either green or blue light. The scaffolds with functionalised CNPs showed better cytocompatibility than the scaffold with plain CNPs.

The PCL scaffold with plain CNPs was also tested for antibacterial activity (in comparison with plain PCL nanofibers) using the strains of *E. coli*, *S. aureus*, *P. aeruginosa* and *E. faecalis*. However, no antibacterial effect was found.

A substantial part of the thesis is also focused on the synthesis of mesoporous carbon particles via soft- and hard-templating. The materials were analysed using SEM and gas adsorption analyses. Selected synthesised materials were functionalised using the above mentioned amide-amine functionalisation and characterised using OEA and gas adsorption. These materials are to be used for grafting on plasma treated polymer surfaces.

Keywords: carbon nanomaterials, functionalisation, tissue engineering, cytocompatibility, amine

ANOTACE

Výzkum materiálů vhodných pro tkáňové inženýrství patří mezi rychle se rozvíjející oblasti; pro kultivaci buněk jsou, mimo jiné, úspěšně požívány různé uhlíkaté materiály. Bylo prokázáno, že adheze a proliferace buněk závisí na mnoha faktorech, jako například přítomnost určitých funkčních chemických skupin, smáčivost povrchu, jeho povrchová energie, morfologie, mechanické vlastnosti apod.

Tato práce představuje nový typ funkcionalizace, při němž byl povrch uhlíkatých nanomateriálů modifikován amid-aminovými skupinami. Velikost a struktura částic byly zkoumány transmisní elektronovou mikroskopií. Specifický měrný povrch a objem pórů byl stanoven pomocí dusíkové adsorpce a vypočten z Brunauer-Emmet-Tellerovy rovnice. Chemické složení připravených materiálů bylo zkoumáno prostřednictvím rentgenové fotoelektronové spektroskopie a organické elementární analýzy, teplotní stabilita pomocí diferenční snímací kalorimetrie.

Funkcionalizované částice byly navázány na povrch polymerních povrchů z polyethylentereftalátu a vysokohustotního polyethylenu, aktivovaných argonovým plasmováním. Chemické složení modifikovaných povrchů bylo analyzováno pomocí Ramanovy a rentgenové fotoelektronové spektroskopie a měřením elektrokinetického potenciálu. Drsnost povrchu byla měřena pomocí mikroskopu atomárních sil, jeho smáčivost pak měřením kontaktního úhlu. Adheze a proliferace potkaních hladkosvalových buněk na modifikovaných površích byla zkoumána *in vitro*.

Výše zmíněné funkcionalizované uhlíkaté nanočástice byly dále využity k přípravě kompozitních nanovlákenných nosičů z polykaprolaktonu. Tyto materiály pak byly porovnávány s čistými polykaprolaktonovými nanovlákny a nanovlákenným kompozitem, obsahujícím pouze neupravené uhlíkaté částice. Struktura připravených nosišů byla zkoumána skenovacím elektronovým mikroskopem, specifický měrný povrch stanoven pomocí dusíkové a kryptonové adsorpce. Cytokompatibilita byla studována v rámci MTT testování na linii 3T3 myších fibroblastů. Vzorky byly dále obarveny pro fluorescenční mikroskopii, během níž při ozařování modrým a zeleným světlem došlo u vzorků obsahujících uhlíkaté částice k tepelnému natavení nanovlákenné polymerní matrice. Nosiče s funkcionalizovanými uhlíkatými částicemi vykazovaly mnohem vyšší cytokompatibilitu než vzorek s neupravenými částicemi.

Dále byly testovány antibiotické vlastnosti nosiče obsahujícího neupravené částice (v porovnání s čistými polykaprolaktonovými nanovlákny) za použití bakteriálních kmenů *Escherichia coli*, *Staphylococcus aureus*, *Pseudomonas aeruginosa* and *Enterococcus faecalis*. Žádná antibakteriální aktivita nebyla prokázána.

Podstatná část práce je též zaměřena na syntézu mezoporézních uhlíkatých materiálů pomocí soft a hard templátování. Připravené materiály byly analyzovány pomocí skenovací elektronové mikroskopie a dusíkové adsorpce. Vybrané materiály byly dále funkcionalizovány výše zmíněným způsobem a charakterizovány za použití organické elementární analýzy a dusíkové adsorpce. Tyto materiály jsou určeny pro budoucí experimenty s navazováním částic na polymerní povrchy pro tkáňové inženýrství.

Klíčová slova: uhlíkaté nanomateriály, funkcionalizace, tkáňové inženýrství, cytokompatibilita, amin

Contents

1. INTRODUCTION

Carbon materials can be found literally everywhere, widely used from home to industrial settings (Hirsch, 2010; Inagaki et al., 2014). The versatility of carbon stems from its ability to form three hybridisation types, which leads to a huge variety of allotropes of either natural or artificial origin (Falcao and Wudl, 2007; Enyashin and Ivanovskii, 2014). Countless carbon-based composites have been prepared and investigated, the interest in this area being not declining for sure, still providing scientists with new challenges.

From the broad spectrum of carbon-based materials, this work focuses *only* on activated carbon nanoparticles (CNPs) and mesoporous carbon materials. If suitably functionalised, their unique properties may be improved and tailored for specific applications. In this work, functionalisation of commercially available CNPs and synthesis of templated mesoporous carbon nanostructures and their functionalisation are primarily aimed at the field of tissue engineering, but the products might also find their use in catalysis and other areas.

Because of a highly interdisciplinary nature of this study, the author believes that, to thoroughly understand the issue, it is essential to manage and participate in as many procedures as possible. Starting with synthesis of the materials, continuing with the production of fibrous materials and plasma treatment, she also aims at analysing and testing via gas physisorption, basics of tissue engineering and fluorescence microscopy.

2. OBJECTIVES

The aim of this work is to prepare and/or modify carbon nanostructures with functional groups that would potentially be useful in tissue engineering and possibly other fields, such as catalysis. For such carbon materials' modifications, a novel type of functionalisation with amide-amine groups was selected. This kind of functionalisation should improve the materials' cytocompatibility, making their surface more suitable for cell adhesion. The influence of various oligoamines, varying in the number and type of amino groups and the length of alkyl chains, will be studied.

After the first experiments with the surface modification of commercially available carbon nanoparticles, prepared templated mesoporous carbon materials could also be used as substrates for functionalisation.

Such structures shall be grafted on plasma treated polymers and tested *in vitro* for cell adhesion and proliferation. Grafting with functionalised carbon nanostructures should enhance the wettability of such polymer surfaces, modify surface roughness and provide the presence of chemical functional groups that support cell adhesion and proliferation.

The functionalised CNPs could also be incorporated into nanofibrous scaffolds, which would be tested *in vitro* for cell adhesion and proliferation. Properties of the prepared materials will be analysed using various analytical methods.

Besides the aims regarding the synthesis and functionalisation, one of the author's main aims is to manage and practice the majority of skills needed to conduct this study. Among others, these shall include production of fibrous materials, plasma treatment, gas physisorption, tissue engineering basics and fluorescence microscopy.

3. THEORETICAL PART

Chapter 3.1. Tissue Engineering contains general information about the topic and describes cell-material interaction. The importance of some specific factors influencing cell adhesion, such as polarity/wettability, electrical charge and conductivity, presence of certain chemical functional groups, surface roughness and topography, is highlighted there (Bacakova et al., 2007, 2011).

Chapter 3.2. focuses on carbon materials in tissue engineering and biomedicine. Chapters 3.2.1.-3.2.7. are aimed at reviewing basic characteristics, usage and functionalisation strategies of activated carbon, fullerenes, graphene, carbon nanotubes, nanodiamonds, nanohorns and dots. Chapter 3.2.8. reviews the issue of cytotoxicity of carbon nanomaterials.

4. RESULTS AND DISCUSSION

4.1. Functionalisation of Commercially Available Carbon Particles

For this part, commercially available active carbon nanoparticles Darco KB-G from Aldrich (batch 4769TH) were used as a substrate. Although the supplier claims that the particle size shall be around 45 μm or larger, the TEM measurements showed that the particles were about 20 to 40 nm in diameter (see Fig. 6 in chapter 4.1.1.). The adsorption-desorption isotherms obtained from nitrogen adsorption measurements represent Type H2 hysteresis loop, which is typical for micro-mesoporous carbon materials (Thommes et al., 2015). The pore size distribution (PSD) was calculated using Density Functional Theory (DFT), for which the slit/cylindrical pore model was chosen as the most suitable, and the PSD plot can be seen later in chapter 4.1.4., Fig. 7.

Generally, the surface of activated carbon is covered with various oxygen groups, such as carboxyl groups, lactones, phenols, carbonyls, anhydrides, ethers or quinones (Figueiredo et al., 1999), the schematic drawing of which can be seen in Fig. 1.

The general scheme of the procedure used for amide-amine funcionalisation can be seen in Fig. 2 and the detailed descriptions of each step are mentioned later in this chapter. Briefly, the CNPs were first oxidised with $(NH_4)_2S_2O_8$. The carboxylic groups thus formed were then chlorinated using thionyl chloride. The acyl chloride thus formed further reacted with oligoamines to form amide-amine groups. The list of the oligoamines used for functionalisation and the names of the corresponding materials prepared can be seen in Tab. 1, the structures of particular amide-amine functional groups grafted on CNPs in Fig. 3.

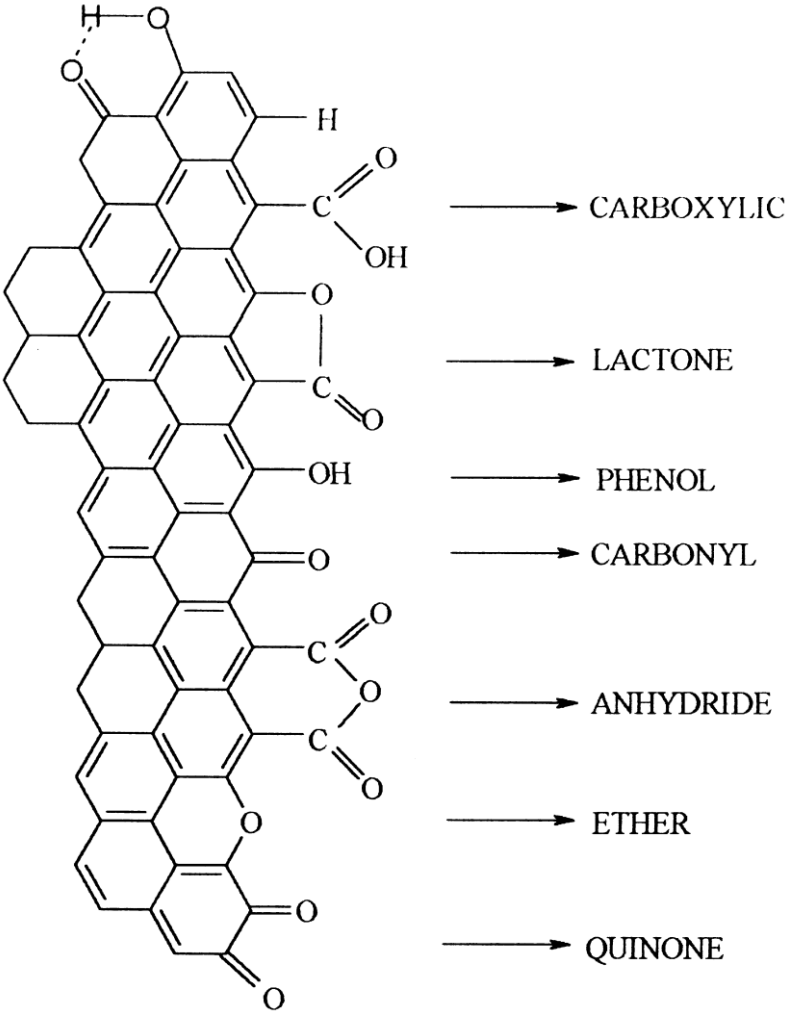

Fig. 1: Surface oxygen groups present on activated carbon (Figueiredo et al., 1999).

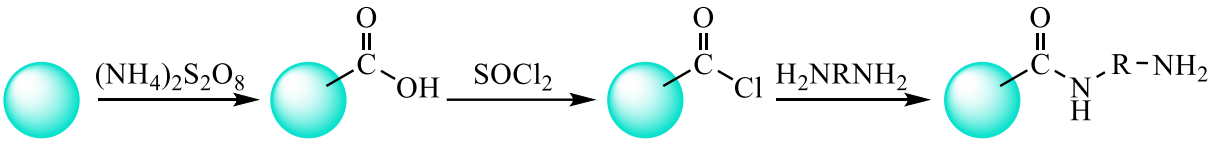

Fig. 2: The scheme of amide-amine functionalisation.

	The oligoamine used	The material's name
a)	hexamethylenediamine	C-HMD
b)	ethylenediamine	C-ED
c)	diethylenetriamine	C-DET
d)	triethylenetetramine	C-TET
e)	tris(2-aminoethyl)amine	C-TAE
f)	tris[2-(methylamino)ethyl]amine	C-TMAE

Tab. 1: The list of the oligoamines used for functionalisation and the corresponding materials prepared.

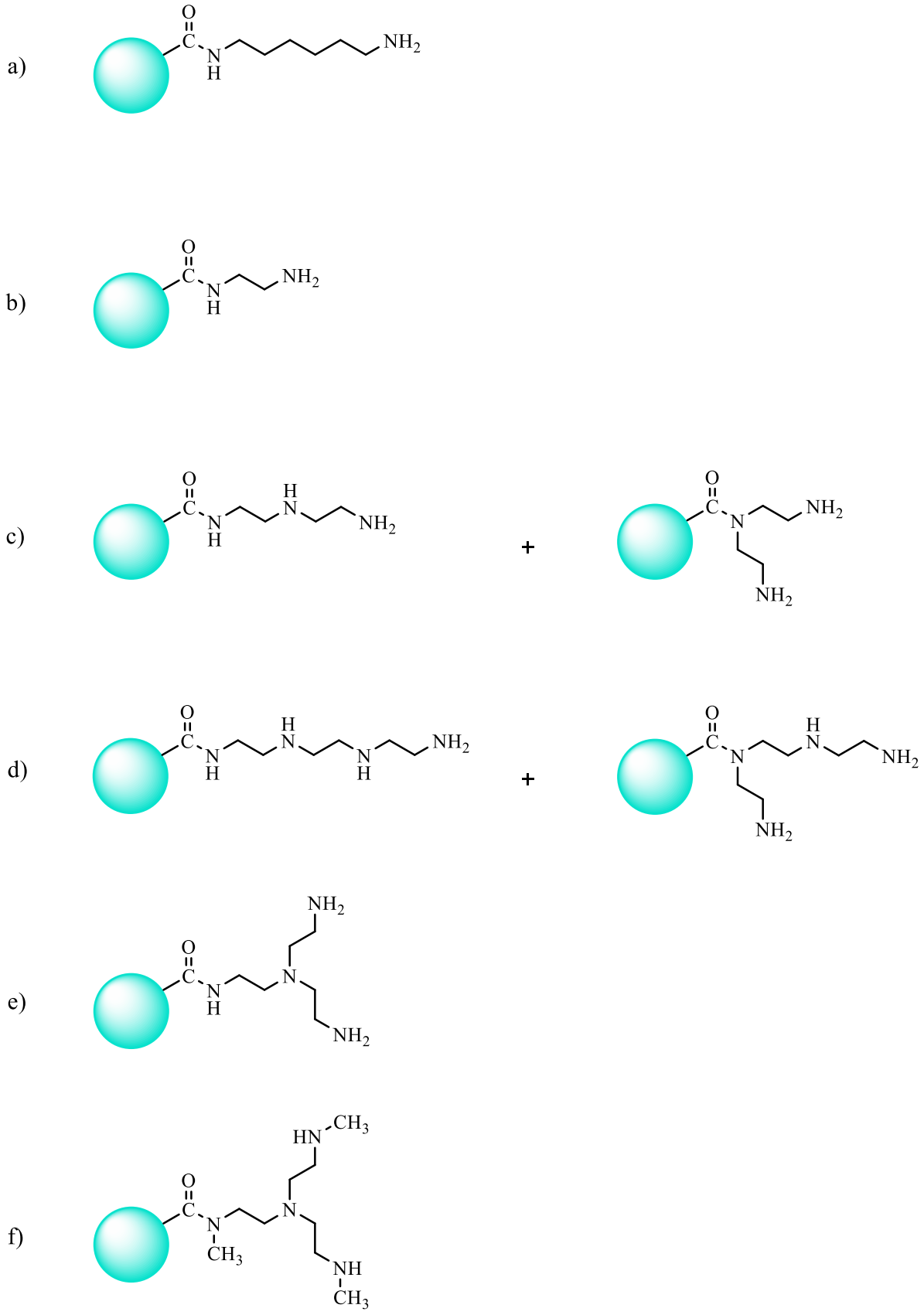

Fig. 3: Structures of particular amide-amine functional groups grafted on CNPs.

There are many methods to oxidise carbon materials, using e.g. O_2 or O_3 atmosphere, hydrogen peroxide, nitric acid or ammonium persulfate (Gómez-Serrano et al., 1994; Jaramillo et al., 2010; Guedidi et al., 2013). However, for the purpose of this work, a method leading mainly to formation of carboxylic groups was essential. Wet methods using HNO_3 and $(NH_4)_2S_2O_8$ have been proved to work this way (Haydar et al., 2003; Lemus-Yegres et al., 2007). As the method using $(NH_4)_2S_2O_8$ described in (Lemus-Yegres et al., 2007) was considered well reproducible and most straightforward, it was selected as the starting step of the functionalisation procedure.

Another step, i. e. conversion of the carboxylic groups into chlorides, was performed via nucleophilic substitution, resp. addition/elimination, using thionyl chloride (Fig. 4). As the carboxylic acid attacks thionyl chloride, a chloride ion leaves, resulting in the formation of oxonium ion, which is activated towards nucleophilic attack. The oxonium ion is then attacked by chloride ion, and a tetrahedral intermediate chlorsulfite is formed. Chlorsulfite then collapses, losing sulphur dioxide and chloride ion, ending up as a protonated acyl chloride. The hydrogen proton can be removed by chloride ion, forming HCl and leaving acyl chloride.

The advantage of using thionyl chloride is that the byproducts of this reaction are gaseous and can therefore be separated easily. The excess of thionyl chloride is removed by distillation.

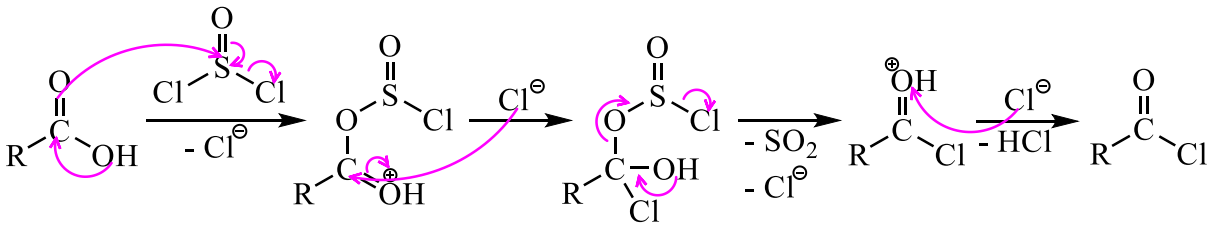

Fig. 4: The reaction scheme of the chlorination step.

Generally, the reaction of an acyl chloride with an amine proceeds in a similar addition/elimination manner (Fig. 5). At first, there is the nucleophilic attack of the lone electron pair on a nitrogen atom of the amine on the partially positive carbon atom of the acyl chloride. With the double bond reformed, the chloride ion is eliminated, which can then remove a hydrogen ion on nitrogen, forming HCl, immediately reacting with the excess of an amine to form alkylammonium chloride. However, a hydrogen can also be removed from the nitrogen directly by an amine.

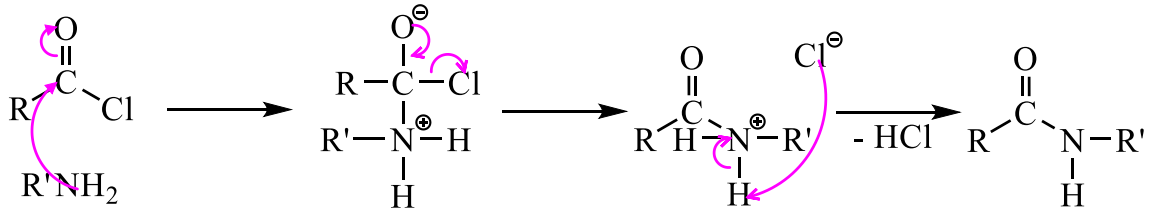

Fig. 5: The reaction scheme of the reaction of acyl chlorides with amines.

Due to the mechanism of such a reaction with oligoamines, it is advisable to use the oligoamines in a high excess, which facilitates the acylation on the primary amino group while surpressing the multiple acylation at the same time.

4.1.1. Transmission electron microscopy

There were no significant visible differences in the structure of the particles; the functionalised CNPs, however, seem to be less sharp. The size of the CNPs can be estimated from the images, varying from 20 to 40 nm (Švorčík et al., 2014). Functionalisation improved wettability of the CNPs and therefore facilitated preparation of CNPs suspension in water.

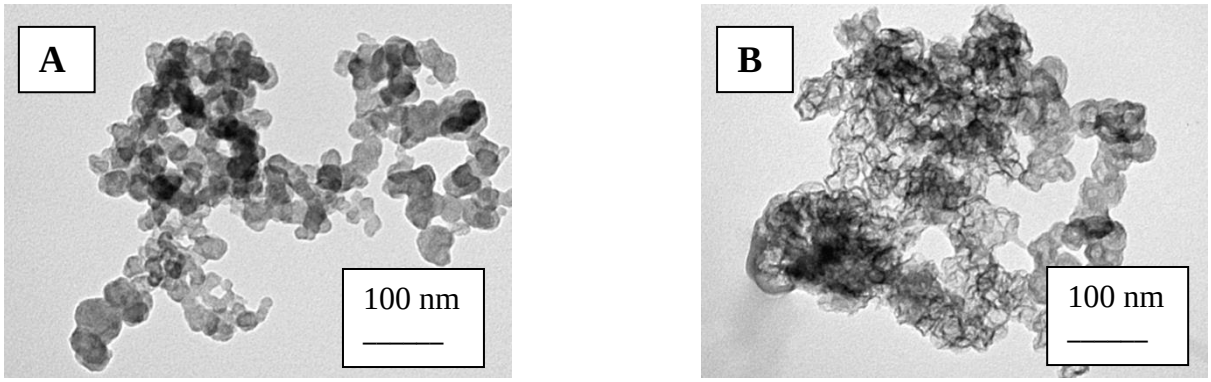

Fig. 6: TEM images of pristine (A) and functionalised (B) CNPs.

4.1.2. X-ray photoelectron spectroscopy

The chemical composition of 6–8 atomic layers on CNP surface was determined, the results of which can be seen in Tab. 2. Nitrogen, chlorine and sulphur were introduced into the structures by functionalisation; an increase in nitrogen concentration on the CNP surface indicates a successful introduction of amino groups onto the CNPs surface. Trace amounts of chlorine on the CNP surface are a result of an incomplete –COCl conversion during the functionalisation process.

	Pristine C	**C-ED**	**C-DET**	**C-TET**	**C-TAE**	**C-TMAE**
Element			**XPS** [at. %]			
C (1s)	89.30	77.06	73.49	78.67	66.37	80.17
N (1s)	-	7.12	10.73	7.44	12.93	4.38
O (1s)	10.70	11.30	14.81	10.90	17.53	12.31
Cl (2p)	-	2.00	0.57	1.77	2.02	1.31
S (2p)	-	2.52	0.40	1.22	1.15	1.83

Tab. 2: Results of XPS measurements of atomic concentrations of C(1s), N(1s), O(1s), Cl(2p) and S(2p)for pristine and functionalised CNPs (ethylenediamine, C-ED; diethylenetriamine, C-DET; triethylenetetramine, C-TET; tris(2-aminoethyl)amine, C-TAE; tris[2-(methylamino)ethyl]amine, C-TMAE).

In the case of C-ED, the results might indicate that this least branched and shortest oligoamine may mostly be positioned in pores of the CNPs.

In the case of acylation of primary amino groups of DET and TET, the linear structures on C-DET and C-TET may also be partially positioned in the pores of CNPs. However, in the case of acylation of secondary amino groups, which is much less likely, the more branched structures shall rather be located on the very surface.

As for the high amount of nitrogen in the case of C-TAE, it can be assumed that these results may have stemmed from the combination of three primary amino groups, which positively influenced the process of acylation, and the overall higher weight ratio of N/C in this branched oligoamine.

On the other hand, as it had been expected, the reaction did not proceed well with the secondary amino groups of the most branched TMAE. The weight ratio of N/C in TMAE was also lower in comparison to the other oligoamines used. The combination of these features resulted in the lowest amount of nitrogen on the surface of C-TMAE.

The lower amounts of nitrogen on C-TET and C-TMAE surfaces correspond with the results of organic elemental analysis (see Tab.8).

To observe the differences between the composition on the very surface and of the lower layers, the following experiment was performed using CNPs functionalised with triethylene tetramine (Švorčík et al., 2014): the analysis was first carried out without Ar^+ ion etching and then after 5 min of Ar^+ ion etching (ions energy 5 keV), as 5 min etching should remove a few nanometres thick surface layer. After ion etching, the concentration of both nitrogen and oxygen decreased by 4.9 % and 10.6 % respectively, which confirms that the functionalisation took place mainly on the very surface of the CNPs (Tab. 3).

	Element atomic concentrations [at. %]					
	Etching time [min]					
	C (1s)		**0 (1s)**		**N (1s)**	
	0	**5**	**0**	**5**	**0**	**5**
Pristine CNPs	97.8	98.5	3.2	1.5	-	-
C-TET	75.5	91.0	15.0	4.4	9.5	4.6

Tab. 3: Results of XPS measurements of atomic concentrations of C(1s), O(1s) and N(1s) for pristine and CNPs functionalised with triethylenetetramine (C-TET) without and after 5 min Ar^+ ion etching.

4.1.3. Organic elementary analysis

The results of OEA can be seen in Tab. 4. As it has already been mentioned, nitrogen and sulphur were introduced into the structures by functionalisation. The lower amount of nitrogen in the functionalised CNPs structures of C-TET and C-TMAE suggest that the amines in question may be bonded in lower amounts due to their three-dimensional arrangements (Žáková et al., 2016) and secondary amino groups.

	Pristine C	C-ED	C-DET	C-TET	C-TAE	C-TMAE
Element			**OEA** [wt. %]			
C	77.76	58.90	56.65	67.74	58.50	64.44
N	-	11.31	11.33	5.67	11.82	6.01
S	-	0.72	0.74	1.79	0.73	1.32
H	2.55	4.37	4.61	3.69	5.02	4.42

Tab. 4: Results of OEA of the pristine (pristine C) and functionalised CNPs (ethylenediamine, C-ED; diethylenetriamine, C-DET; triethylenetetramine, C-TET; tris(2-aminoethyl)amine, C-TAE; tris[2-(methylamino)ethyl]amine, C-TMAE).

After a few successfully functionalised batches, some new batches seemed to have slightly different properties, which caused problems with grafting the functionalised CNPs on plasma treated polymer surfaces (see chapter 4.2.). The results of OEA showed that such batches contained cca twice as much nitrogen in comparison to the original nitrogen content (which was about 82 wt. %). After a thorough evaluation of the whole process, the oxidation step was considered the most probable cause.

	C	S	H	N
Sample		**OEA [**wt. %]		
original	81.72	-	3.006	-
2 hours uncooled	73.84	0.577	2.616	-
4 hours uncooled	71.53	0.777	2.631	-
8 hours uncooled	71.03	0.769	2.725	-
12 hours uncooled	70.85	0.680	2.794	-
24 hours uncooled	68.07	0.454	2.735	-
48 hours uncooled	67.22	0.394	2.834	-
30 minutes cooled	77.83	-	2.867	-
60 minutes cooled	76.89	-	2.935	-
90 minutes cooled	77.67	-	2.951	-

Tab. 5: Results of OEA of newly oxidised CNP samples.

When checking the composition of newly oxidised samples (named 24 hours uncooled) via OEA, it was found that the new samples were ‘overoxidised’ in comparison to the original batches. The procedure was therefore optimised using various times of oxidation and cooling. Examples of the OEA results can be seen in Tab. 5, the adjusted procedure is described in the thesis in chapter 5.1.3.

It also seemed that $(NH_4)_2S_2O_8$ used for oxidation of the first batches might not have been as strong an oxidation agent (possibly e.g. due to storage conditions). Nevertheless, the procedure was successfully optimised, using always a freshly opened batch of $(NH_4)_2S_2O_8$ and cooling. The more oxidised a sample, the lower the carbon content in the sample was, as oxidation introduced more oxygen into the structures (mainly carboxylic groups, as it has been discussed earlier in chapter 4.1.). Surface area and pore size distribution changes are discussed in the following chapter.

4.1.4. Surface area, pore size distribution and pore volume analysis

Because oxidation may result in changes in the porous structure of the material, which can then affect its behaviour (Jaramillo et al., 2010), PSDs of pristine, oxidised and functionalised CNPs were measured and can be seen in Fig. 7. As mentioned before in chapter 4.1., the adsorption-desorption isotherms obtained from nitrogen adsorption measurements represent Type H2 hysteresis loop, which is typical for micro-mesoporous carbon materials (Thommes et al., 2015). The pore size distribution (PSD) was calculated using Density Functional Theory (DFT), for which the slit/cylindrical pore model was chosen as the most suitable.

As can be seen in Fig. 7, oxidation did not significantly change the pore size distribution. However, due to oxidation, the surface area decreased by 199 $m^2\ g^{-1}$. A noticeable change in both PSD and surface area can be observed for C-TET, the surface area of which decreased by more than 1130 $m^2\ g^{-1}$ in comparison to pristine C. The PSD of C-TET followed the trend similar to pristine and oxidised CNPs, nevertheless, a prominent decrease in microporosity and pores with diametres above 8 nm can be seen. Slit/cylindrical DFT pore model fitted well to all three samples in Fig. 7.

Results of surface area and pore volume analyses of the pristine and functionalised CNPs can be seen in Tab. 6. Functionalised samples were degassed at 150 °C for several hours, then adsorption and desorption isotherms were measured with nitrogen. Five points Brunauer–Emmett–Teller (BET) analysis was applied for the total surface area determination and 40 points Barrett–Joyner–Halenda (BJH) model for pore volume (Žáková et al., 2016). The functionalisation caused a distinct decrease in the total surface area from 1518 $m^2\ g^{-1}$ (for unmodified CNPs), which indicates the coverage of the surfaces by the grafted amines. In addition, the pore volume decrease confirmed the amines grafted onto CNPs surface and into their pores.

Pristine C	**ED**	**DET**	**TET**	**TAE**	**TMAE**
Surface area [$m^2\ g^{-1}$]					
1518	74.2	156.5	386.1	150.4	81.4
Pore volume [$cm^3\ g^{-1}$]					
0.602	0.154	0.264	0.420	0.349	0.169

Tab. 6: Results of surface area and pore volume analyses of the pristine (pristine C) and functionalised CNPs (ethylenediamine, ED; diethylenetriamine, DET; triethylenetetramine, TET; tris(2-aminoethyl)amine, TAE; tris[2-(methylamino)ethyl]amine, TMAE).

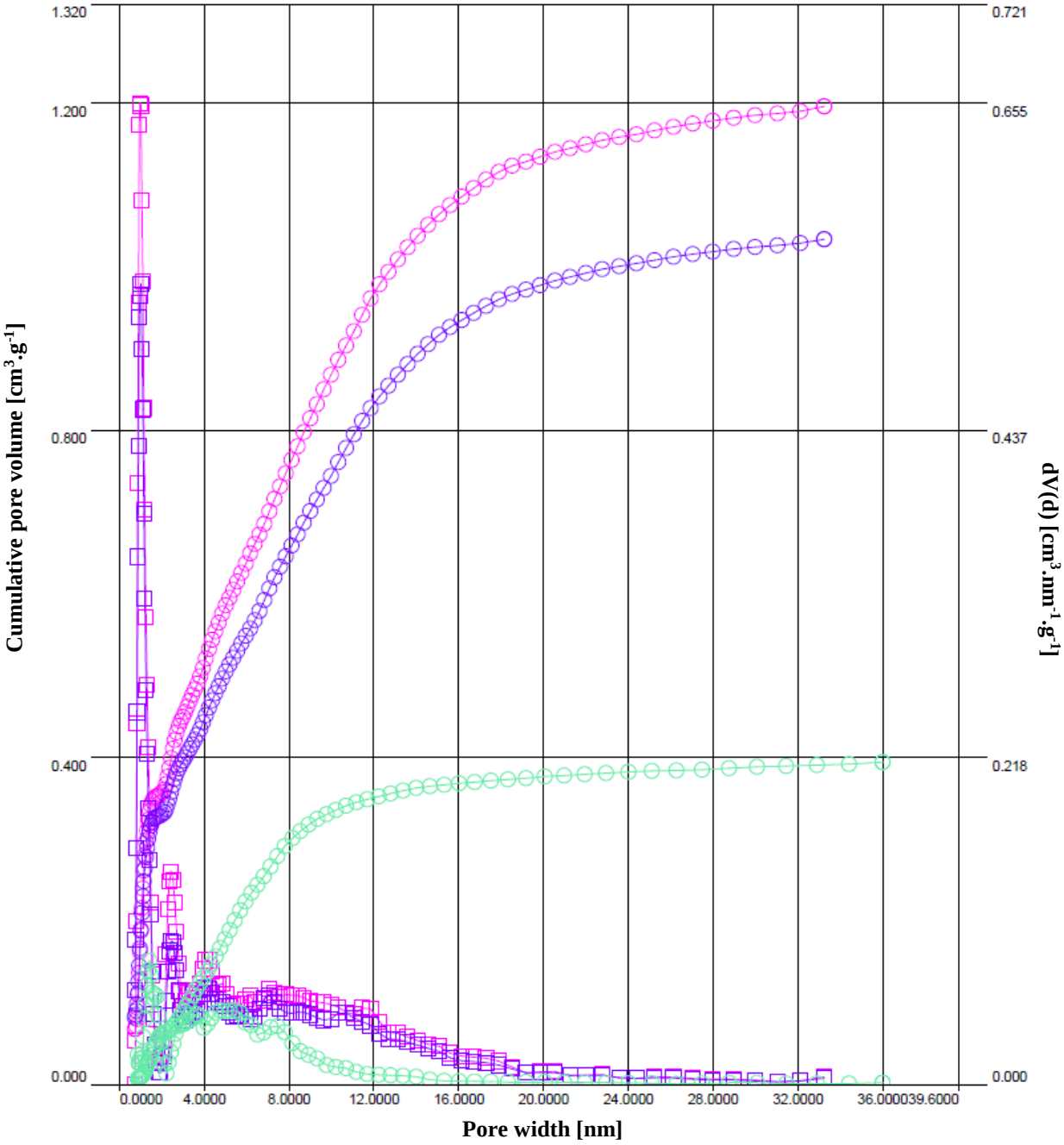

Fig. 7: The pore size distribution curves of pristine CNPs (magenta), oxidised CNPs (violet) and C-TET (green).

4.1.5. Electrokinetic analysis – zeta potential

Colloidal samples of CNPs (0.01 g) dispersed in KCl water solution (4 ml of 0.01 mol l^{-1}) were tested by dynamic light scattering. The electrokinetic analysis, the results of which can be found in Tab. 7, also confirmed the successful grafting of amino-compounds onto the CNP surface. While the zeta potential of pristine CNPs of −10.5 mV is negative, zeta potential of all amino-grafted CNPs shifted to positive values. There is a good correlation between the amounts of amino-groups in grafted molecules and the shift of the surface charge to positive values (Žáková et al., 2016). It is known that the presence of amino groups on CNP surface results in zeta potential increase and shifting to the positive values (Reznickova et al., 2012).

Pristine C	ED	DET	TET	TAE	TMAE
		Zeta potential [mV]			
-10.5	15.9	19.4	21.3	27.5	21.0

Tab. 7: Results of electrokinetic analysis of the pristine (pristine C) and functionalised CNPs (ethylenediamine, ED; diethylenetriamine, DET; triethylenetetramine, TET; tris(2-aminoethyl)amine, TAE; tris[2-(methylamino)ethyl]amine, TMAE).

4.1.6. Differential scanning calorimetry

Differential scanning calorimetry was used to examine the thermal stability of the pristine and functionalised CNPs. The measurements were performed in a range of 25–1000 °C in oxygen at a flow rate of about 50 ml/min. The heating/cooling rate was 10 °C/min. DSC peak for the pristine CNPs at 445 °C is shifted to slightly higher temperatures for modified samples. This can be explained by a decrease in CNPs surface area during the treatment. Degradation/oxidation of amine groups starts above approx. 150 °C and the relevant parts of DSC curves differ depending on the amines used. In the case of pristine TET (not bonded with CNPs), complete degradation bellow 210 °C was observed (Silva et al., 2012). Our observation of a broad bump (see Fig. 8) with a tiny maximum at 250 °C for TET modified CNPs thus demonstrates chemical bonding of TET on CNPs (Žáková et al., 2016).

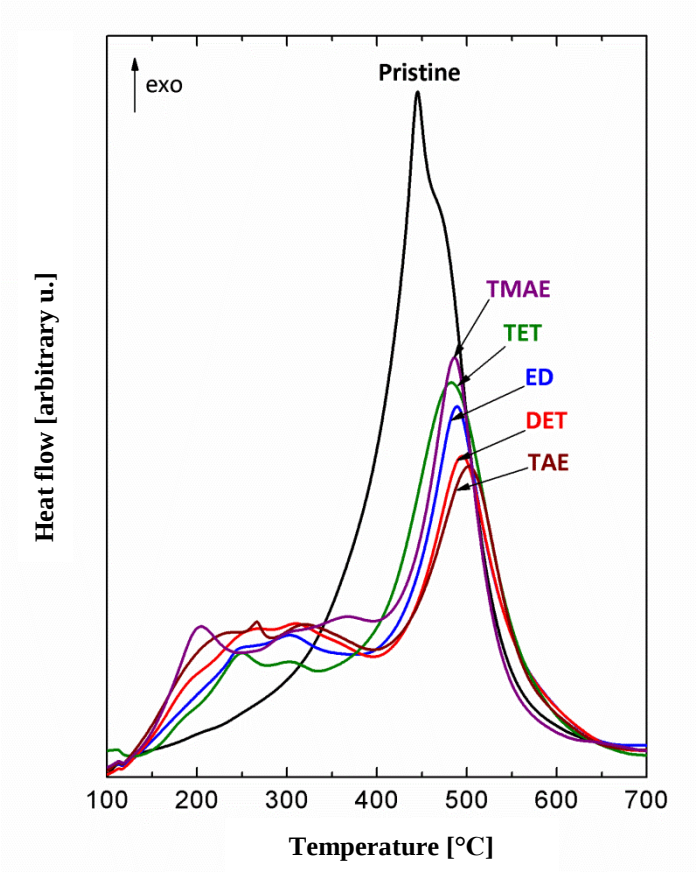

Fig. 8: *DSC scans* of *the pristine (pristine C) and functionalised CNPs (ethylenediamine, ED; diethylenetriamine, DET; triethylenetetramine, TET; tris(2-aminoethyl)amine, TAE; tris[2-(methylamino)ethyl]amine, TMAE).*

4.2. Grafting of the functionalised CNPs on polymer surfaces and their cytocompatibility testing

As this part was not the author's own work, the results will be described only briefly. The detailed information about the research can be found in the following articles: (Trostová et al., 2013, 833; Švorčík et al., 2014; Žáková et al., 2016). The scheme of the experiments is depicted in Fig. 9.

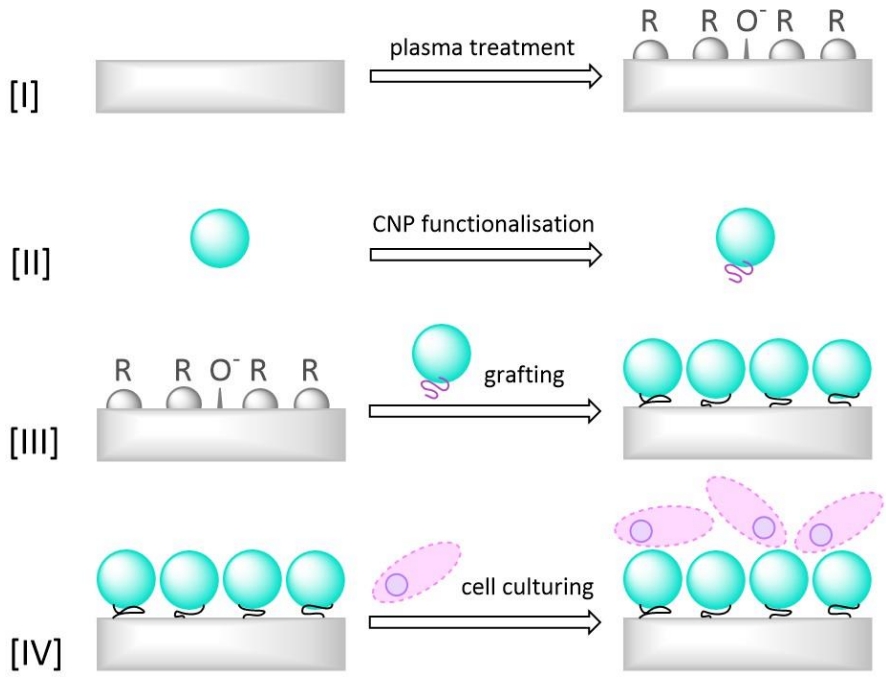

Fig. 9: The scheme of the experiments: [I] Ar plasma treatment of a polymer, [II] functionalisation of CNPs, [III] grafting of functionalised CNPs on the plasma treated polymer, [IV] cytocompatibility testing

The functionalised CNPs were chemically grafted on polyethylene terephthalate and high density polyethylene the surfaces of which had been treated with argon plasma. The chemical composition of the modified polymer surfaces was determined by Raman and X-ray photoelectron spectroscopies. Graphitic peaks attributed to CNPs could be observed in Raman spectra. The presence of nitrogen on the very surface of the materials was confirmed by means of angle resolved XPS.

Surface roughness and morphology of polymers grafted with CNPs was studied by atomic force microscopy, surface contact angle was measured by goniometry. AFM images showed that the CNPs were spread relatively homogeneously on the polymer surface, however, they did not form a continuous coverage. As the functionalisation improved wettability of the CNPs surfaces, the wettability of the polymers grafted with functionalised CNPs also increased, which can be indicated from the decrease in water contact angle.

Adhesion and proliferation of vascular smooth muscle cells on HDPE and PET surfaces grafted with functionalised CNPs were studied *in vitro*. Functionalised CNPs grafting on the plasma activated polymers had a positive effect on VSMCs adhesion and proliferation. In comparison with pristine, plasma treated or methanol etched surfaces there was a significant increment in

the numbers of cultivated cells on the substrates grafted with CNPs. The viability of cells cultivated on all grafted types of functionalised CPs was extremely high. In all cases (except for the 1st day, on which the cells were still adapting to modified surface), the cell viability was above 95 %. However, there were no significant differences in the numbers of cultivated cells among the individual types of the grafted CNPs (Žáková et al., 2016). We can therefore assume that the structure of the amino chains did not play an important role in cell adhesion. Some deviations were caused by various parts of the samples being covered more densely.

To sum up this set of experiments, it can be stated that grafting PET and HDPE with amide-amine functionalised CNPs had positive effects on cytocompatibility of these polymers with VSMCs.

4.3. Nano-microfibrous Scaffolds Containing Carbon Particles

Four types of nanofibrous scaffolds containing the aforementioned particles were prepared via sputtering CNPs into electrospun polycaprolactone (PCL) micro-nanofibres: three of them with three types of functionalised CNPs (C-ED, C-TAE and C-TMAE) and one with plain activated CNPs. First, a micro-nanofibrous layer was electrospun, on which the particles were sputtered and subsequently covered with another micro-nanofibrous layer.

4.3.1. Surface area

The surface areas of the scaffolds containing CNPs were determined from adsorption and desorption isotherms. Samples were degassed at 40 °C for 24 hours (not to alter the PCL fibres), then adsorption and desorption isotherms were measured with nitrogen or krypton adsorption (Linde, 99.999% purity). Seven points BET analysis was applied for the total surface area determination.

Incorporation of CNPs caused a distinct increase in the total surface area from 4.3 $m^2 g^{-1}$ for pristine PCL nanofibres to 15.9±3.5 $m^2 g^{-1}$ for scaffolds containing the functionalised CNPs and 235.8 $m^2 g^{-1}$ for the scaffold containing the pristine CNPs (see Tab. 8). The surface area increments roughly correlate with the surface areas of the CNPs, except for sample PCL+CTAE. It can be assumed that there might have been a lower amount of the TAE functionalised CNPs, the scaffold might have been thicker (i.e. consisting mainly of PCL fibres) or that the particles were somehow covered with PCL, which could have blocked their accessible surface area. Although there was the same amount of CNPs sputtered into the PCL fibres during electrospinning, electrospinning itself is a highly sensitive process and every little, seemingly insignificant, change may result in noticeable differences in materials' properties.

PCL scaffold exhibited Type II isotherm according to IUPAC classification (Fig.10, squared curve in cyan) (Thommes et al., 2015). Adding CNPs in the structure significantly altered the materials' properties and the hysteresis loops measured resembled H4 type, which is a composite of type I and II isotherms. Such hysteresis loops are typically found with micro-mesoporous carbon materials. PCL+C scaffold can clearly be distinguished from the others (Fig. 10, x curve in apricot), as the volume of adsorbed nitrogen is much higher due to the much larger specific surface area of the pristine CNPs, the surface of which had not been blocked by the amide-amine functions.

Particles	Surface area [m^2 g^{-1}]	Scaffolds	Surface area [m^2 g^{-1}]
pristine C	1058.9	PCL+C	235.8
ED	74.2	PCL+CED	15.5
TAE	150.4	PCL+CTAE	12.9
TMAE	81.4	PCL+CTMAE	19.4
		PCL	4.3

Tab. 8: The results of the surface area analyses of CNPs and PCL scaffolds (ethylenediamine, ED; tris(2-aminoethyl)amine, TAE; tris[2-(methylamino)ethyl]amine, TMAE).

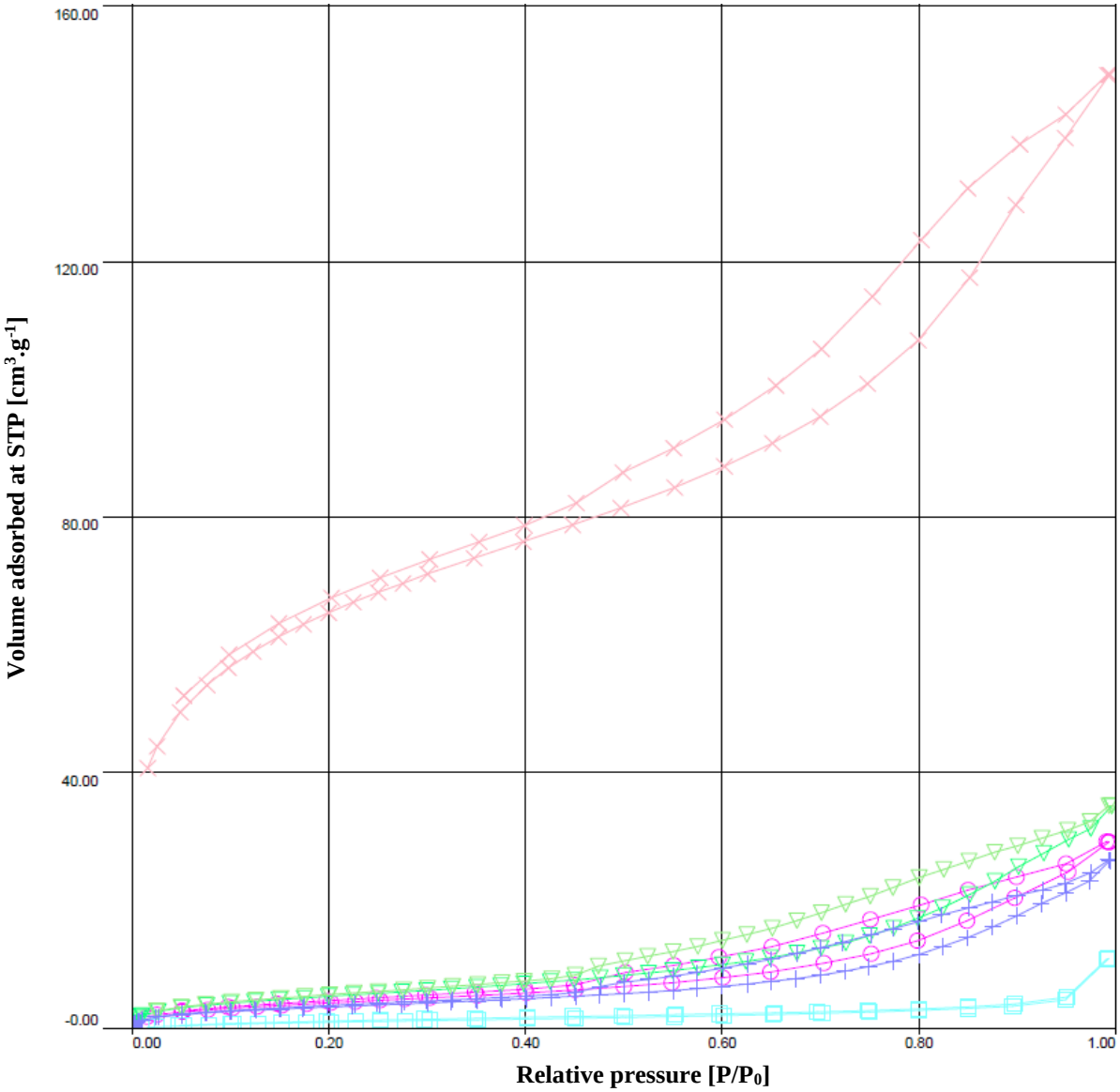

Fig. 10: Adsorption and desorption isotherms for all fibrous scaffolds: PCL (square, cyan), PCL+C (X, salmon), PCL+CTAE (cross, purple), PCL+CTMAE (triangle, green) and PCL+CED (circle, magenta).

4.3.2. Cytocompatibility with 3T3 mouse fibroblasts – MTT assay

The cell viability was estimated via measurements of absorbance of a formazane solution, as formazane is formed when yellow tetrazole 3-(4,5-dimethylthiazol-2-yl)-2,5-diphenyltetrazolium bromide is reduced to purple formazan in living cells by a mitochondrial reductase. As can be seen in Fig. 11, cell adhesion on the first day was similar for all scaffolds except for PCL+C. On day 3, however, pristine PCL scaffold started to overtake the others and on day 8, the absorbance measured for pristine PCL clearly indicated higher cell viability than for the other scaffolds. Nevertheless, the performance of the scaffolds with the functionalised CNPs was also quite good. The results for PCL+C are really poor in comparison to all the other scaffolds, which showed that functionalisation of CNPs had a positive effect on cell adhesion and proliferation. The differences among the individual types of oligoamines are noticeable but not too big. On day 14, pristine PCL was still by far the most suitable material for 3T3 mice fibroblasts while PCL+C seemed to have created the most hostile environment for them. PCL+CED and PCL+CTAE ended almost the same, with moderately good cell viability. Again, the functionalised CNPs exhibited better results than the pristine CNPs.

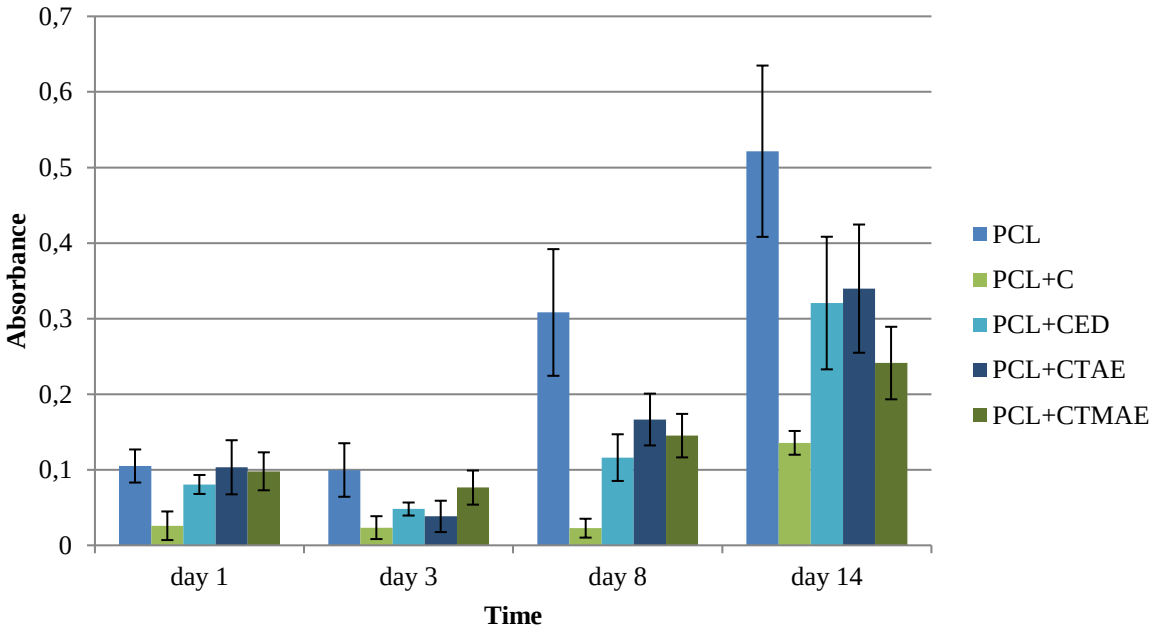

Fig. 11: Results of MTT assay sorted by days.

4.3.2.1. Fluorescent microscopy

The samples were examined via fluorescent microscopy. As more fluorescent dyes were used (propidium iodide and DAPI in combination with phalloidin-FITC), the photographs were taken using UV, blue and green light filters (i. e. emissions at 420 nm, 515 nm and 610 nm, respectively). Generally, when staining one sample with more dyes that are excited at different wavelengths, more photographs are taken, each one using a different filter. They are then collated into one final photograph, in which the cells and their parts shall overlap. A photograph of a cell culture stained with DAPI with phalloidin-FITC can be seen in Fig. 12, which shows the pristine PCL nanofibrous scaffold.

The same procedure was applied to take FM photographs of the other scaffolds, i. e. those containing CNPs. However, the cells and their parts did not overlap in any of the cases. An example of such a phenomenon can be seen in Fig. 13.

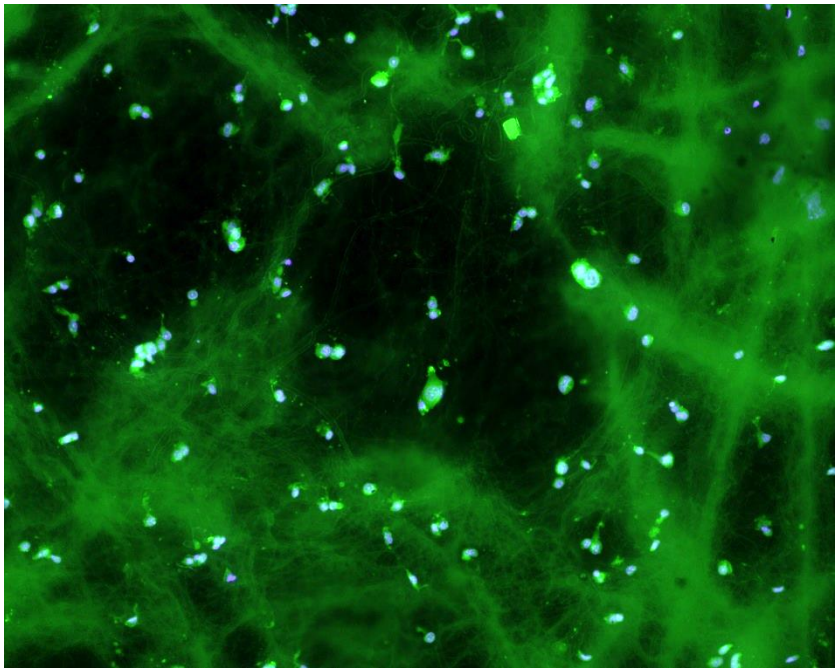

Fig. 12: Fluorescent microscopy photograph of PCL scaffold with 3T3 mouse fibroblasts on day 1, stained with DAPI (nuclei, blue) and phalloidin-FITC (actin fibres, green). Note: the larger green structures are fibres of the PCL scaffold.

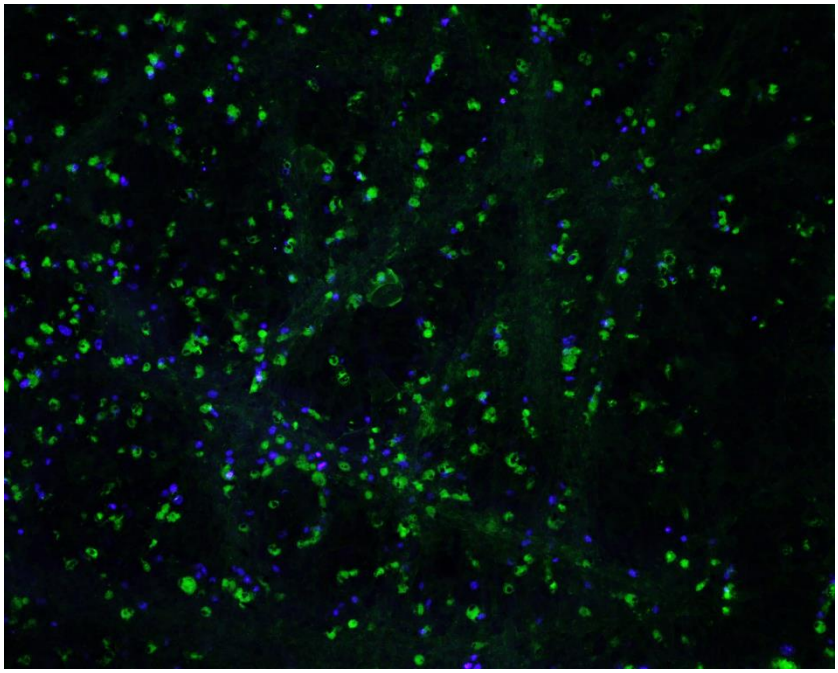

Fig. 13: Fluorescent microscopy photograph of PCL+CTMAE scaffold with 3T3 mouse fibroblasts on day 1, stained with DAPI (nuclei, blue) and phalloidin-FITC (actin fibres, green); the cell nuclei do not overlap with the actin fibres.

As the cells in the images were not *just* shifted in one direction but simply occupied different locations in random directions, it was clear that this phenomenon had not been caused by

a careless manipulation, e. g. moving the samples. As the cells had already been dead, they could not have moved by themselves. The only logical explanation was that something must have happened with the material itself during taking the photographs, causing its morphological changes and thus changing the position of the cells.

It was then found that all scaffolds containing CNPs were sensitive to irradiation when using the blue and green filters. The morphological changes started immediately after the beginning of irradiation, leading to literally tearing the materials and holes formation within a few seconds. It happened to all the scaffolds containing CNPs, regardless the functionalisation. Irradiation with UV light did not have such an effect, which is not surprising considering the fact that carbon materials, especially carbon black, are widely used as UV stabilisers in polymer production.

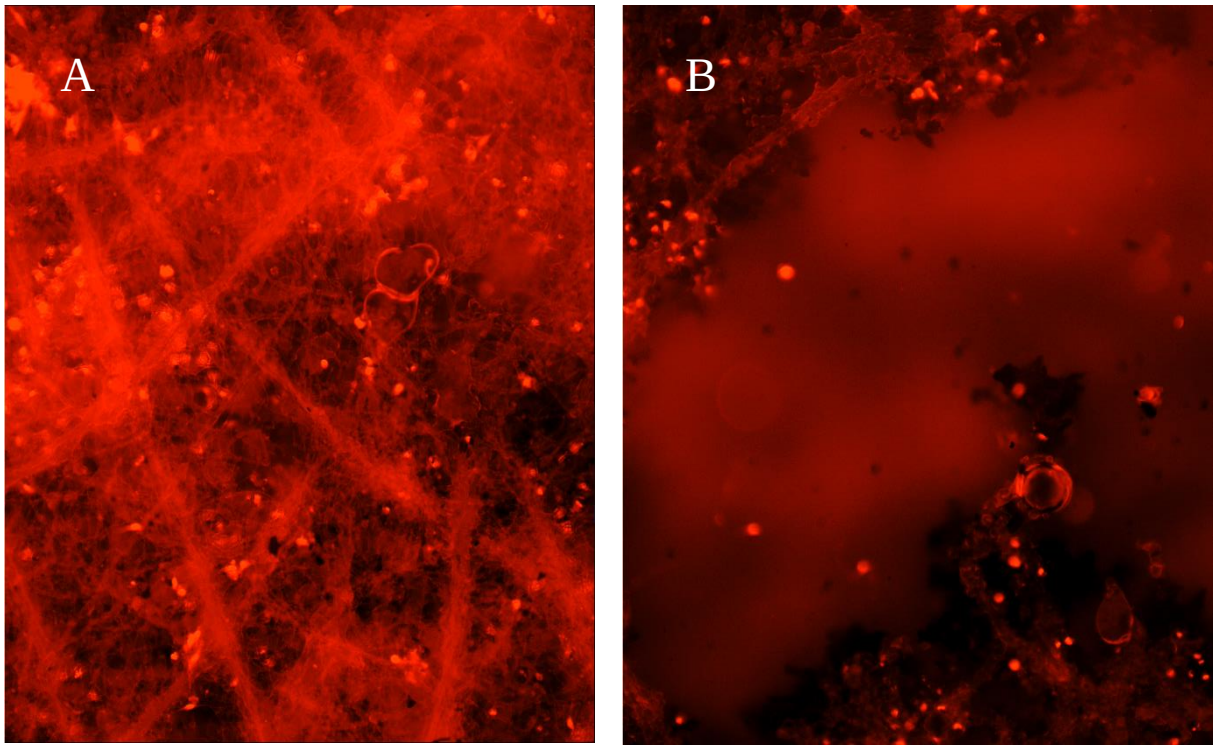

Fig. 14: Fluorescent microscopy photographs of 3T3 mouse fibroblasts on PCL+CTMAE scaffold on day 8 during irradiation with the green filter after: A) 0 seconds, B) 15 seconds

Pictures A and B in Fig. 14 were taken from a short film that had captured a structural degradation of PCL+CTMAE sample in real time. In the film, which can be found on a CD attached to this work, a few changes can be seen during the first seconds, while larger breaks occur in around the tenth second. They then spread wider, joining into one, which continues growing with time.

It was further examined whether the presence of the fluorescent dyes and the overall methodology of FM sample preparation affected the materials' selective light sensitivity. No such effects have been observed.

The CNPs containing scaffolds were also checked using Raman DXR microscope (laser at a wavelength of 532 nm, objective: 10x/0.25 BD). Using the 25 µm pin hole aperture, even with the weakest power, i. e. 2 mW, it took only a few seconds to create holes in the substrates.

4.3.3. Scanning electron microscopy

Although all the scaffolds were prepared at the same conditions, the photographs revealed significant morphological differences among them. While the pristine PCL scaffold can be described as predominantly nanofibrous (Fig. 15), the other ones containing the CNPs were rather microfibrous with some nanofibres present in the structures (Fig. 16). CNPs also aggregated into larger agglomerates during sputtering into the electrospun fibrous layers. The presence of the conductive CNPs might have altered the usual behaviour of the newly developing fibres during the electrospinning process, which is extremely sensitive to even the slightest, seemingly insignificant, alterations in conditions.

The structures of CNPs containing scaffolds after green light irradiation were also studied using SEM. The fibres seemed to have melted, which resulted in creating holes in the materials, as can be seen in Fig. 17.

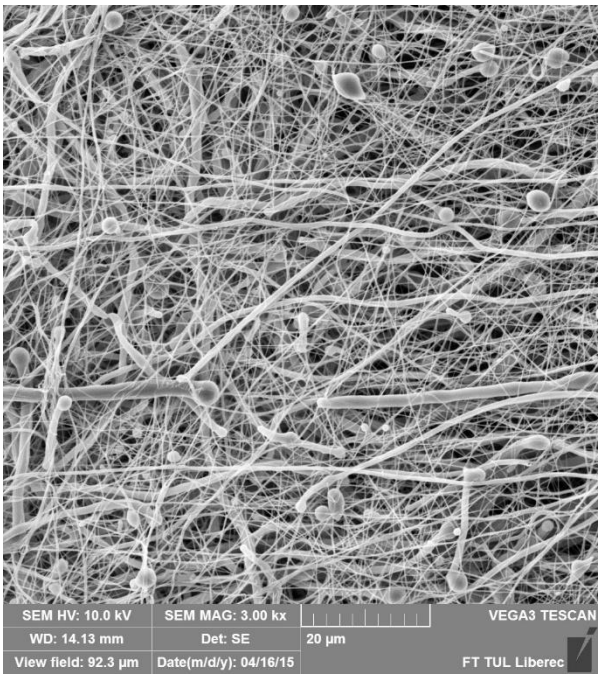

Fig. 15: Scanning electron photograph of PCL nanofibrous scaffold.

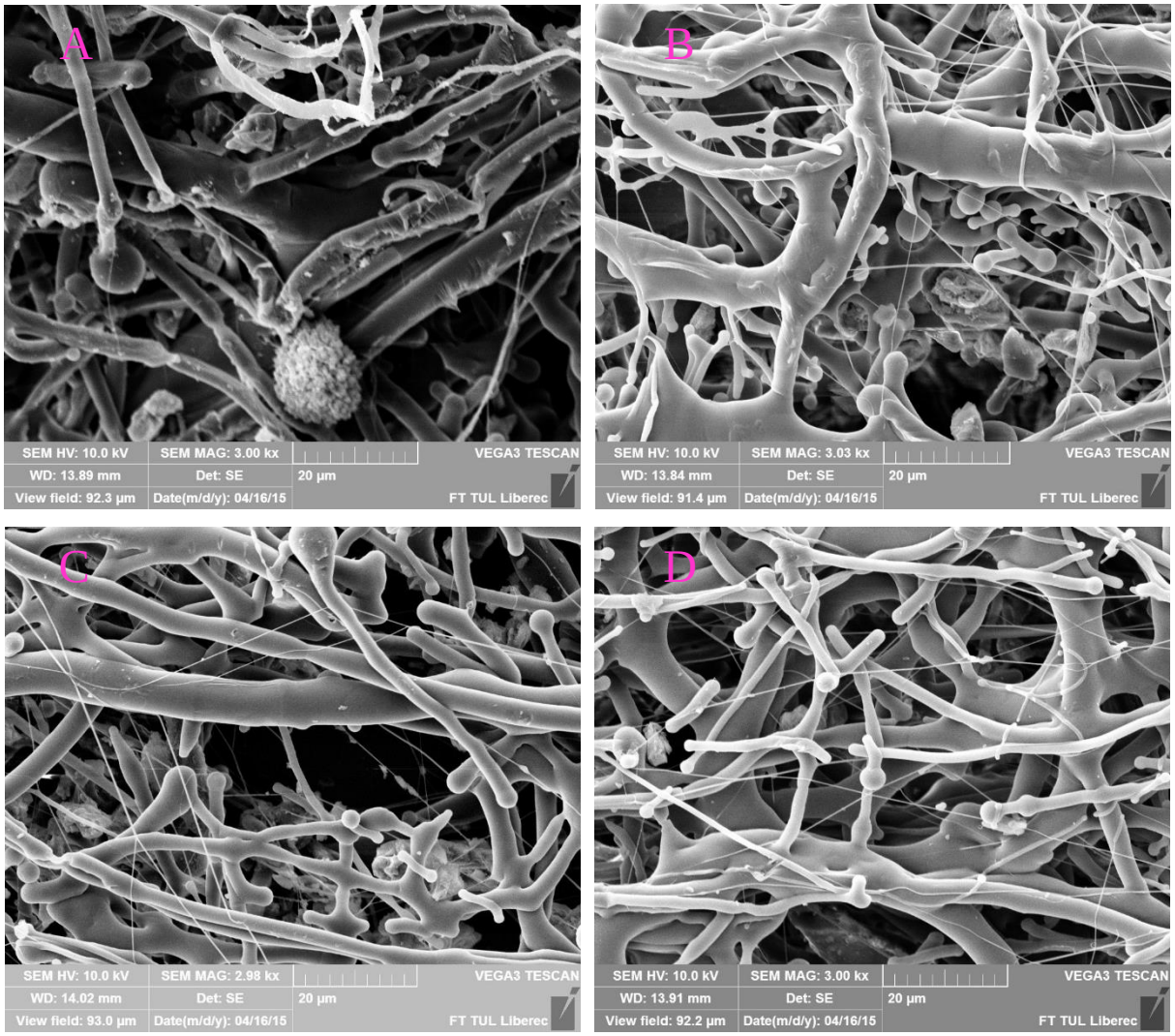

Fig. 16: Scanning electron photographs of PCL micro-nanofibrous scaffolds containing CNPs: A) PCL+C, B) PCL+CED, C) PCL+CTAE, D) PCL+CTMAE.

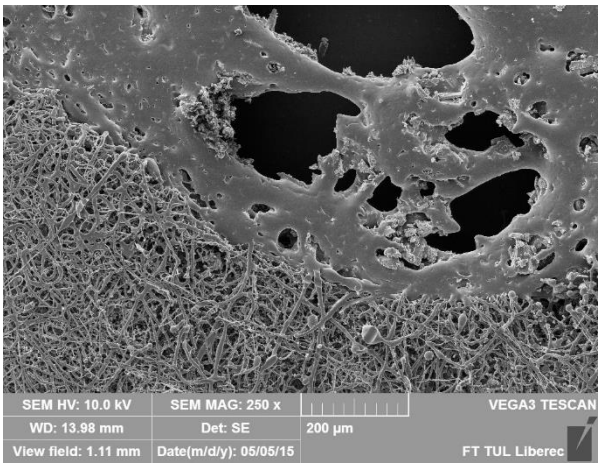

Fig. 17: Scanning electron photographs of a melted part of PCL+CTAE scaffold.

4.3.4. Thermogravimetric analysis

Samples PCL and PCL-C were analysed via thermogravimetric analysis. Cca 10 mg of each material was heated to 650 °C at a rate of 10 °C/min under nitrogen flow at a rate of 60 ml/min. It was then kept at that temperature for 10 min. After that, the sample was exposed to synthetic air with the same flow rate at the same temperature for 15 minutes.

As can be seen in Fig. 18, the carbonisation residue is very low, approximately 0.2 weight %. It is therefore possible to assume that all combustible content from PCL-C at 650 °C may correspond with the amount of carbon present in the fibres. The amount of non-combustible residues for PCL and PCL-C are 1.64 % and 2.25 % respectively. The second significant peak in Fig. 19 can be assigned mainly to oxidation of CNPs, which might have formed cca 25 weight % of PCL-C sample.

Both materials started to decompose at similar temperatures, i.e. above 280 °C. However, the temperature at which the decomposition proceeded at the highest speed was cca 30 °C lower for PCL-C material. The presence of CNPs might facilitate decomposition of PCL in PCL-C in comparison to pristine PCL. However, the slower speed/higher temperature of PCL decomposition in PCL sample may be also influenced by the higher amount of PCL, which may have taken longer to heat and subsequently decompose.

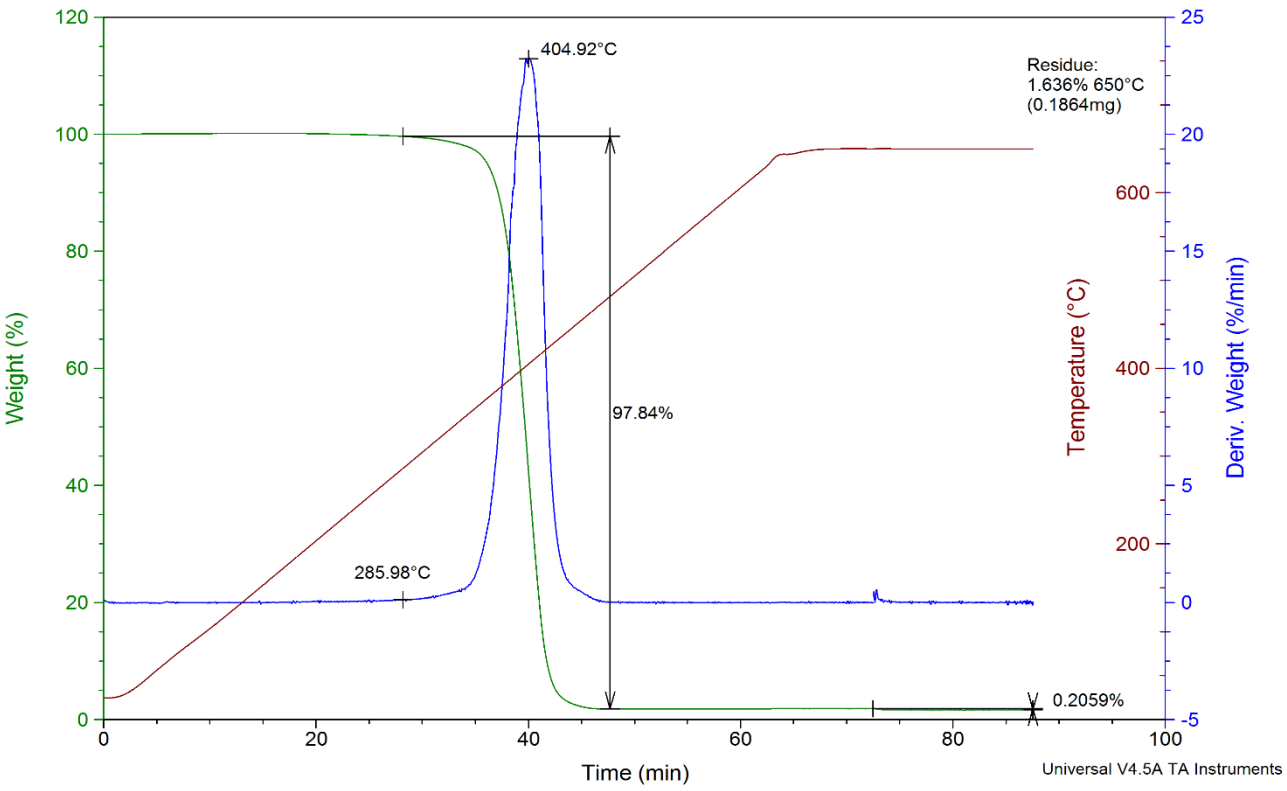

Fig. 18: The TGA plot for PCL nanofibrous scaffold.

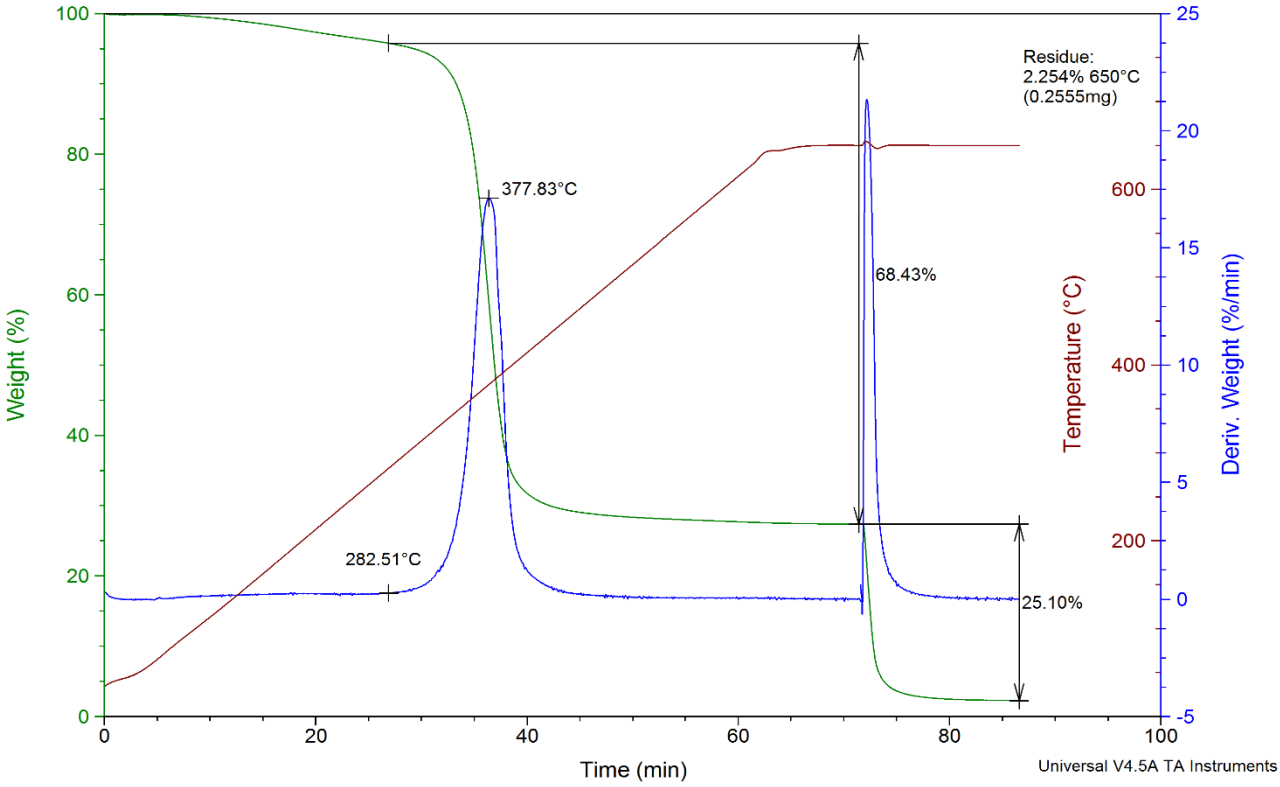

Fig. 19: The TGA plot for PCL+C micro-nanofibrous scaffold.

4.3.5. Differential scanning calorimetry

DSC was used to examine the thermal behaviour of the pristine PCL s and PCL+C scaffolds. The measurements were performed in a range of -20–100 °C in nitrogen at a flow rate of 50 ml/min, the heating/cooling rate was 10 °C/min. The measurements were based on the Boersma and heat flow principles.

The first heating reflected structural properties of a sample, as well as some feature of its preparation, such as solvent residues or different conditions. The measurement showed a non-standard curve for the PCL+C sample; nevertheless, it can be said that a lower energy/temperature was needed to change the structure of PCL+C material in comparison to pristine PCL fibres.

4.3.6. Antibacterial properties testing

Because the cell adhesion and viability of 3T3 mice fibroblasts was very poor on PCL+C sample, an idea whether this composite might exhibit antibacterial properties came into question. Therefore, a series of antibacterial testing experiments was carried out. The procedure was similar to the one described in (Padil et al., 2015). The antibacterial activity of the plain PCL nanofibres and PCL-C scaffold was investigated by a qualitative method determining the zone of inhibition. Using the bacterial strains of Gram-negative *Escherichia coli* and *Pseudomonas aeruginosa* and Gram-positive *Staphylococcus aureus* and *Enterococcus faecalis*, no inhibition zones around the samples were detected. It can be therefore assumed that the nanofibrous scaffolds loaded with CNPs possess no antibacterial effect.

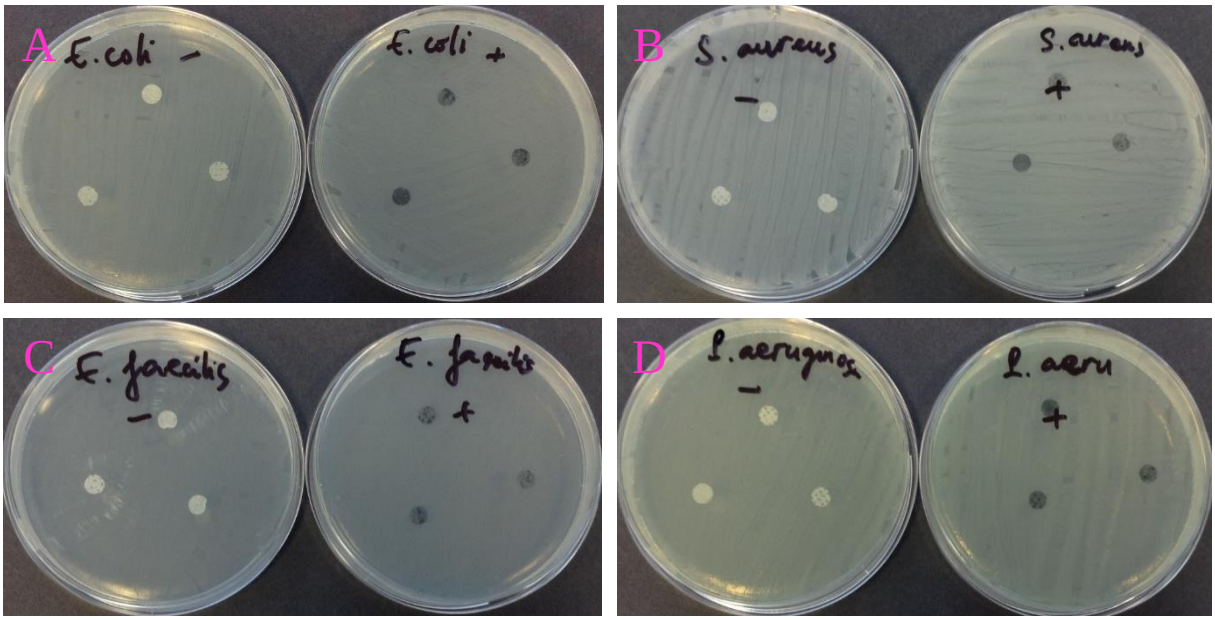

Fig. 20: Photographs of agar plates inoculated with A) E. coli, B) S. Aureus, C) E. faecalis, D) S. Aeruginosa with pristine PCL nanofibers (white, -) and PCL+C micro-nanofibrous scaffolds (black, +).

4.4. Templated Mesoporous Carbon Materials

Several mesoporous carbon materials were prepared via hard- and soft-templating methods. The morphology of all the synthesised materials was studied using SEM.

The surface areas and pore size distributions were calculated using ASiQwin software based on adsorption-desorption isotherms. The pristine and functionalised samples were degassed at 300 °C or 150 °C, respectively, for at least 12 hours, after which nitrogen (Linde, 99.999% purity) 40-point adsorption and desorption isotherms were measured at the temperature of liquid nitrogen. 7-point BET analysis was applied for the total surface area determination. Various models of Density Functional Theory were used for the pore size distribution calculations. The previously widely used BJH model is no longer recommended for such applications in micro-mesoporous materials examination (Thommes et al., 2015), as it can significantly underestimate the pore size for narrow mesopores (for pore diameter smaller than 10 nm the pore size may be underestimated even by 30 %) (Lowell et al., 2012).

4.4.1. Hard-templated Materials

4.4.1.1. Ordered Mesoporous Carbon Materials Based on SBA-15 Silica Template

Two types of mesoporous carbon materials were obtained using SBA-15 as their template: JAK017A, where no boric acid was used, and JAK017B with boric acid used as a pore expanding agent.

SEM photographs did not show any noticeable differences, as can be seen in Fig. 21. However, it can be seen that the materials are porous.

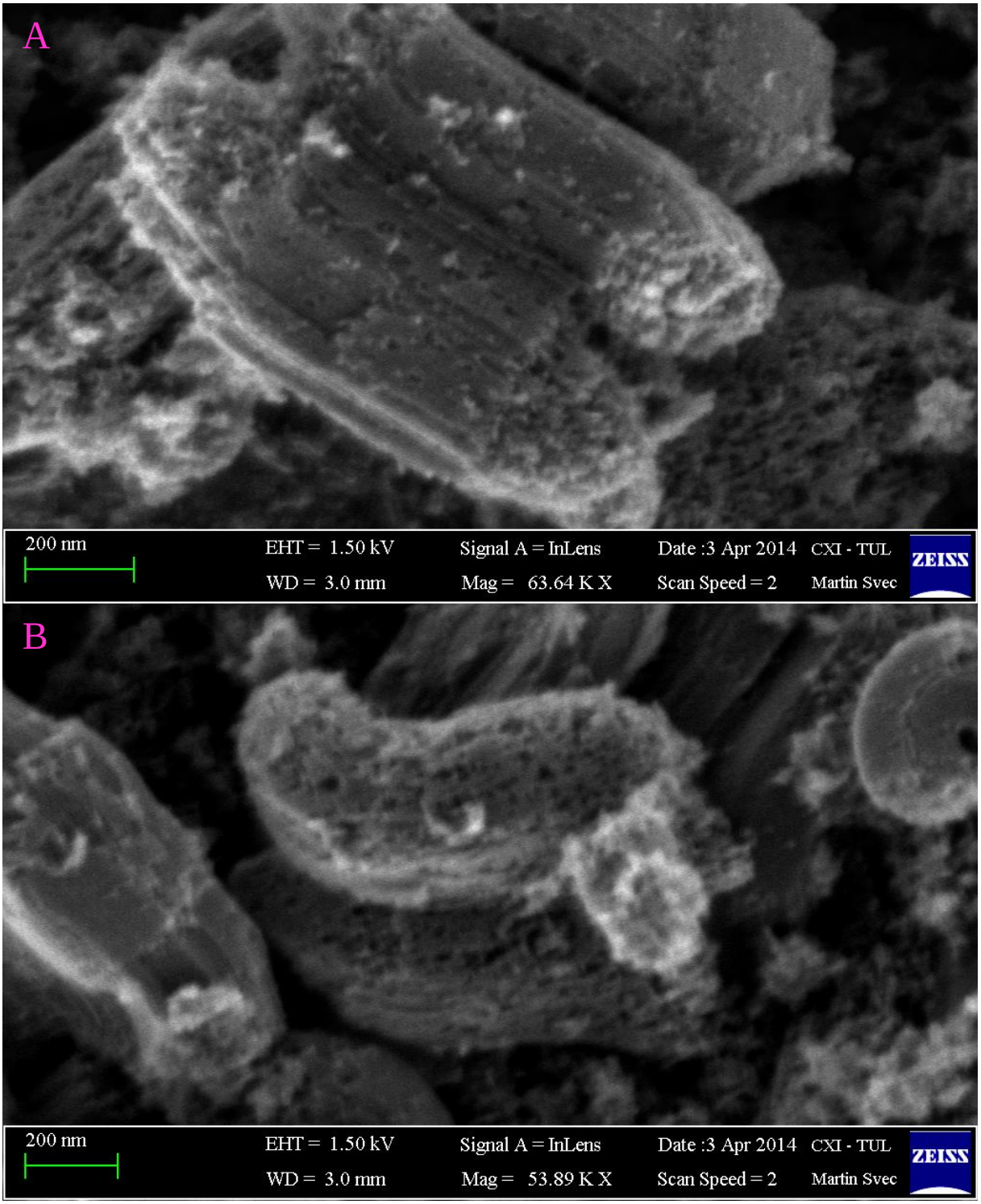

Fig. 21: Scanning electron photographs of JAK017A (A) and JAK017B (B).

Surface area and pore size distribution (PSD) analyses provided more information about the materials' morphology. While the surface area of SBA-15 was 522.4 m^2 g^{-1}, the surface area of JAK017A and JAK017B were much higher, 2234 m^2 g^{-1} and 1927 m^2 g^{-1}, respectively. According to the PSD curve for SBA-15 (in pink), which can be seen in Fig.22, the structure of the material is ordered, with the slightly wider peak at around 11 nm. The structure of JAK017A, represented by the blue curve, can also be considered ordered. There are two

significant narrow peaks, the first one in the micropore region and the second one at around 6 nm. Nevertheless, some wider pores are also present in the structure.

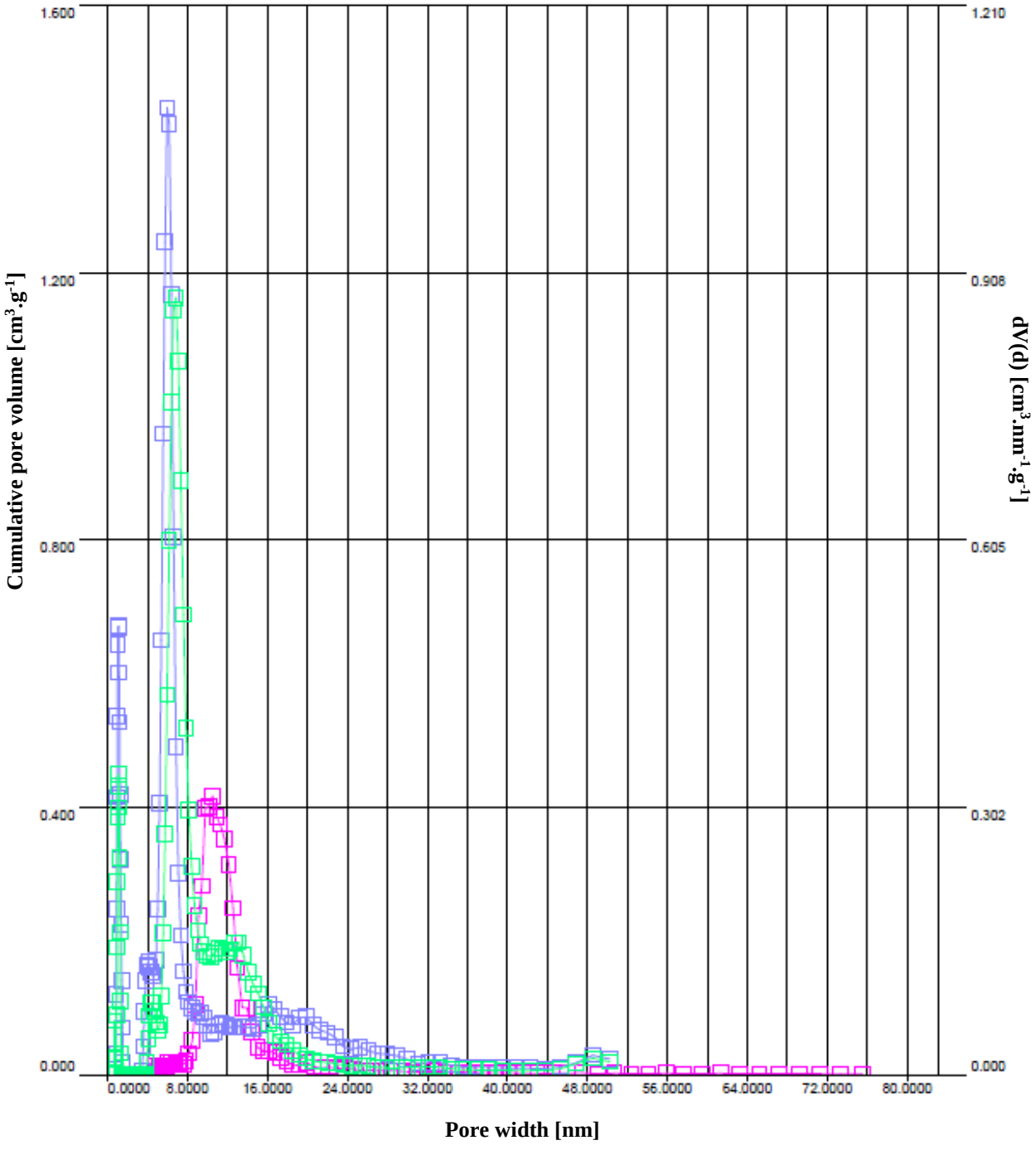

Fig. 22: The pore size distribution curves of SBA-15 (magenta), JAK017A (blue) and JAK017B (green).

The structure of JAK017B (green curve) is also ordered, with one sharp peak in the micropore region, the other at around 6.7 nm, and with some larger pores present. It can be therefore assumed that boric acid worked as the pore expanding agent, indeed. However, the structures are not as highly ordered as they were supposed to be according to (Li et al., 2011), and the

average pore size of JAK017A is larger than that of a corresponding material mentioned in the study.

JAK017B was chosen for further functionalisation.

4.4.1.2. Ordered Mesoporous Carbon Materials Based on Monodisperse Silica Nanospheres (JAK019)

According to SEM photographs in Fig. 23, the template looks monodisperse and the average diameter of the silica nanospheres was 60 nm. The pores in the carbon material, which are based on the nanospheres and can be seen in Fig. 24, are also spherical (which corresponds with the DFT model chosen for the assessment of PSD). However, the PSD is not narrow and the material cannot be considered ordered (Fig. 25).

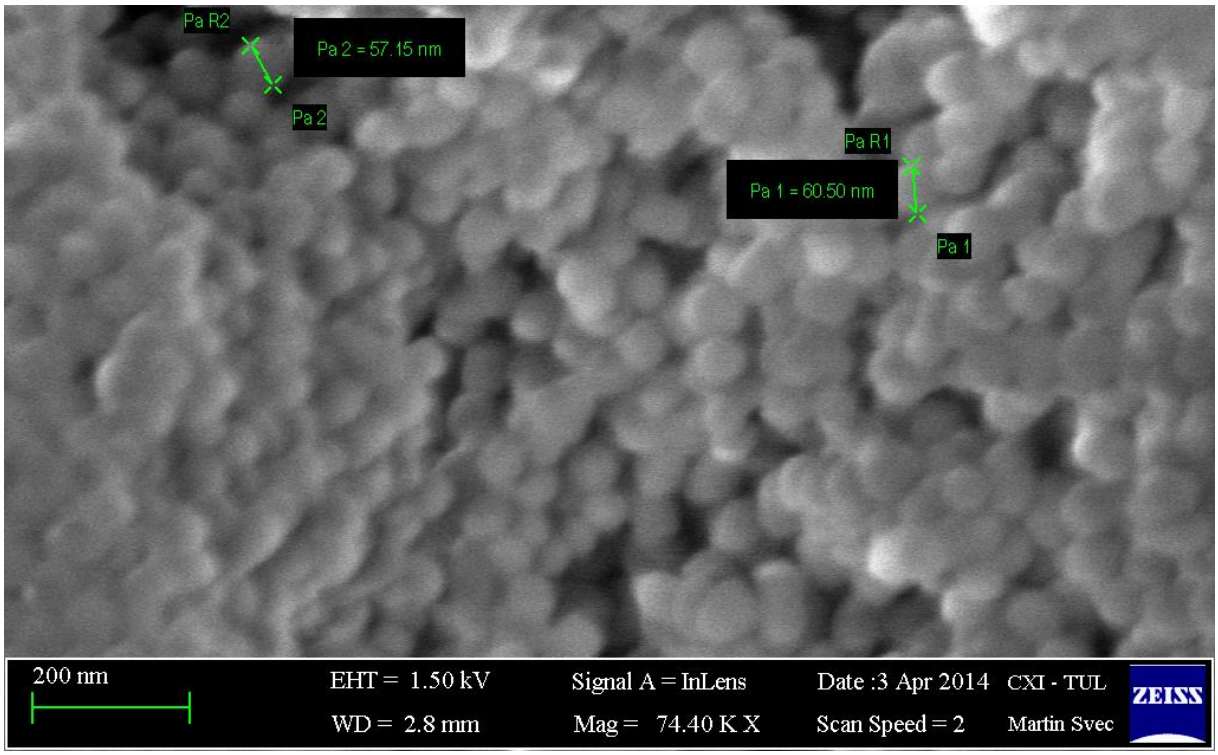

Fig. 23: Scanning electron photograph of the silica template for JAK019.

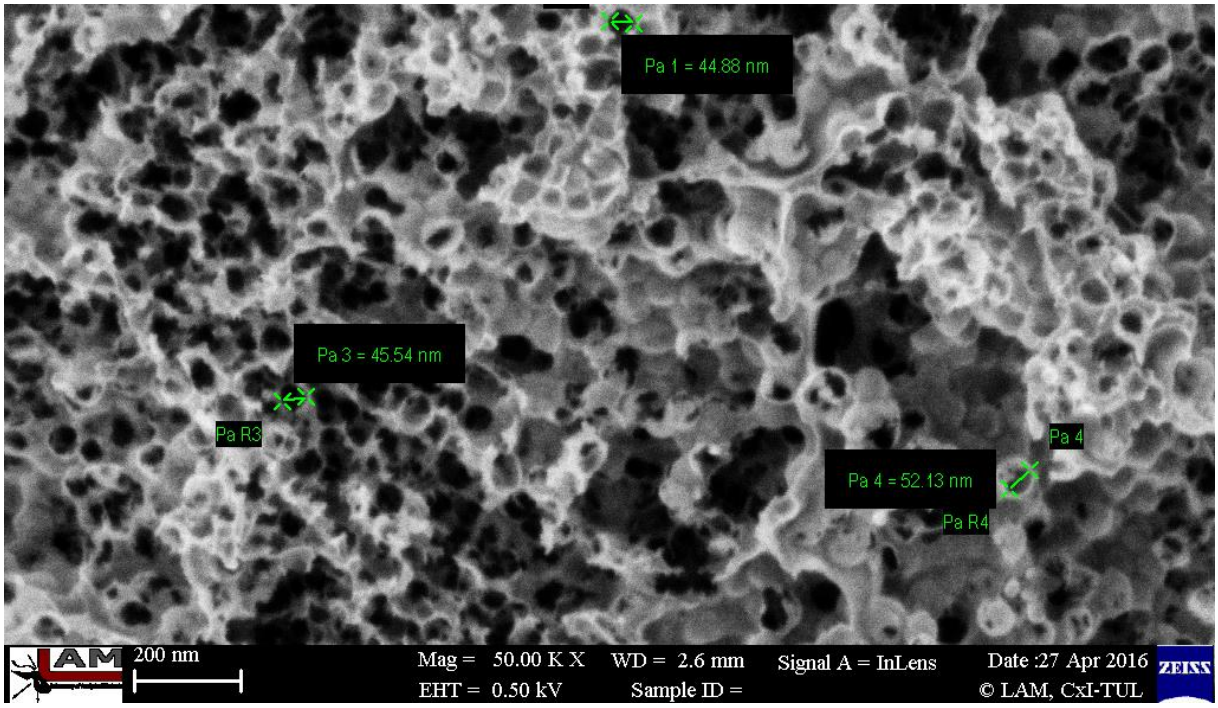

Fig. 24: Scanning electron photograph of JAK019.

The surface area of the material is 155 m^2 g^{-1}, which is not very high, taking into consideration that surface areas of carbon materials commonly exceed 500 m^2 g^{-1}, and even values above 1500 m^2 g^{-1} are not exceptionally high. It is also possible that some silica spheres might have stayed inside their carbon wrapping, which would have increased the weight of the sample and thus made the surface area seem smaller. According to the PSD curve in Fig. 25, micropores and mesopores are present. The overall shape of the hysteresis loop can be described as H3 type, which also suggests the presence of macropores that were not completely filled with pore condensate (Thommes et al., 2015). The presence of macropores would be in accordance with the SEM photograph in Fig. 24.

JAK019 was chosen for further functionalisation.

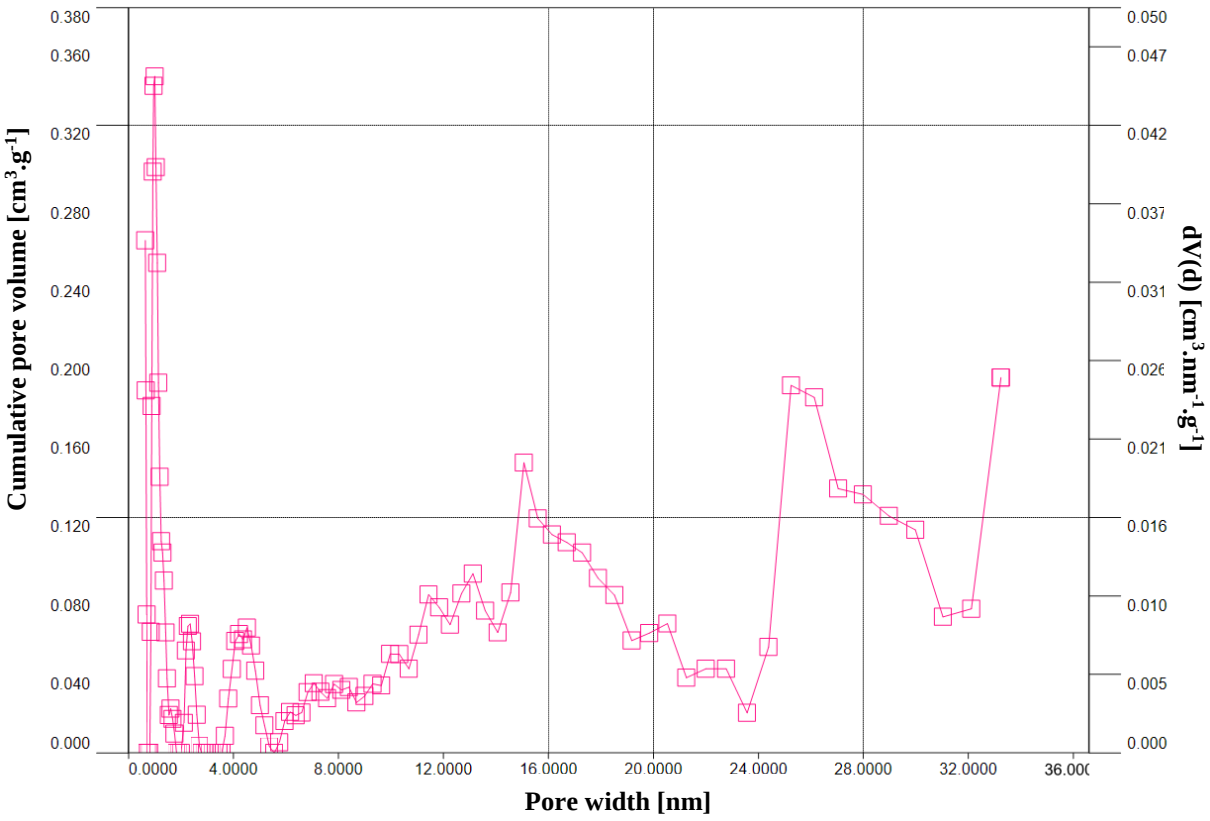

Fig. 25: The pore size distribution of JAK019 based on DFT.

4.4.2. Soft-templated Materials

4.4.2.1. Porous Carbon Nanospheres (JAK045)

Two batches of this material were prepared via a low-concentration hydrothermal synthesis (chapter 5.5.2.1. in the thesis). Although the procedure was the same, the resulting materials, named JAK045A and JAK045B, were different. None of them exhibited either a narrow particle or pore size distribution, as can be seen from the SEM photographs shown in Fig. 26. and PSD curves in Fig. 27. The majority of JAK045A nanospheres were around 40 nm in diameter, but larger particles of cca 120 nm in diameter were also present in the mixture. However, in comparison with JAK045B, the particle size distribution was much narrower; the smallest particles observed in JAK045B were around 70 nm in diameter, while even particles larger than 1 μm in diameter could be found in SEM photographs.

The surface area differed by cca 120 m^2g^{-1} (the surface areas of the batches JAK045A and JAK045B were 617 m^2g^{-1} and 737.3 m^2g^{-1}, respectively).

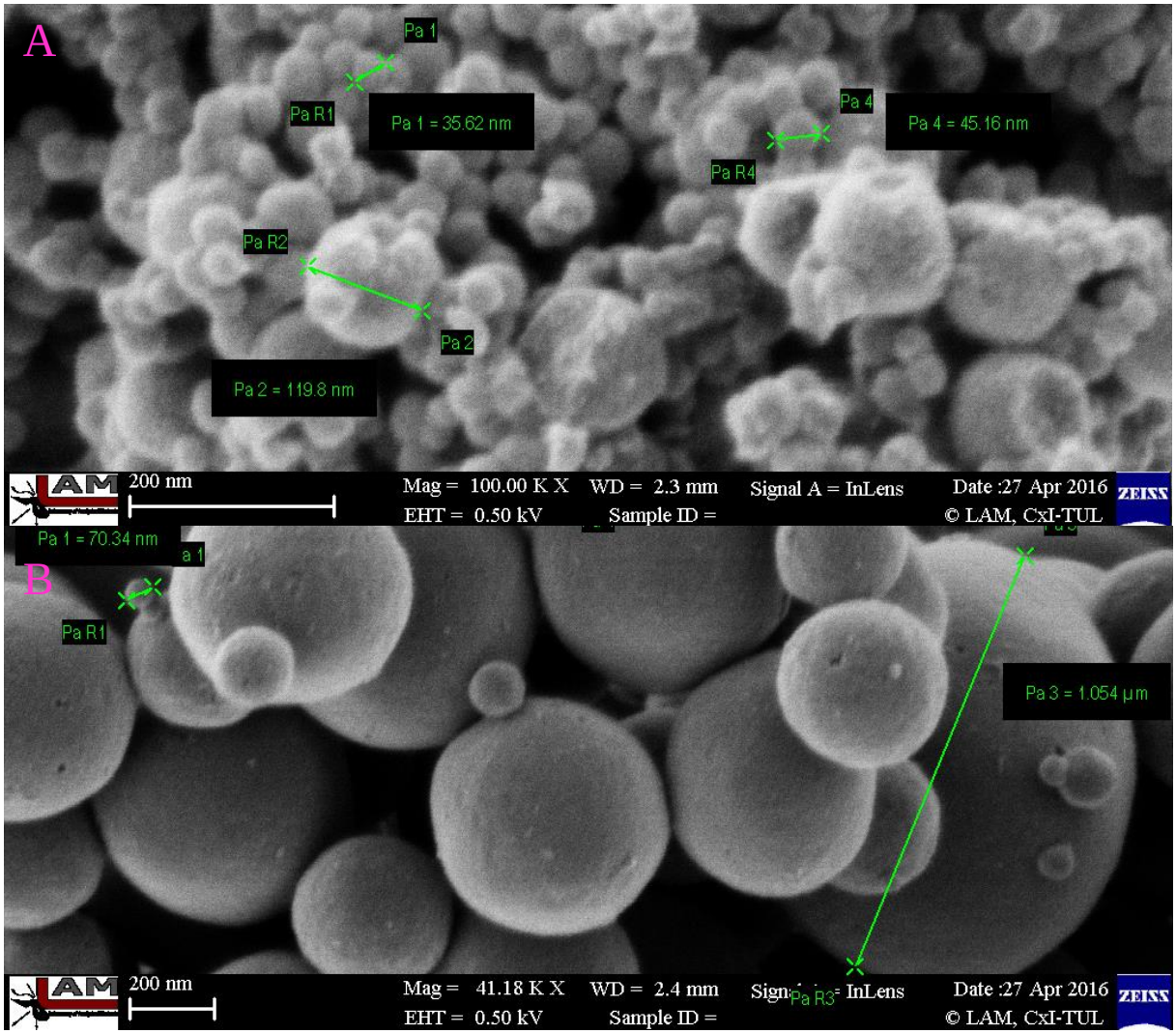

Fig. 26: SEM photographs of JAK045A (A) and JAK045B (B).

These differences could have been caused by the oscillating temperatures during the hydrothermal treatment in the autoclave, which was a drawback impossible to fix in our conditions. Further experiments with this kind of nanospheres were therefore discontinued.

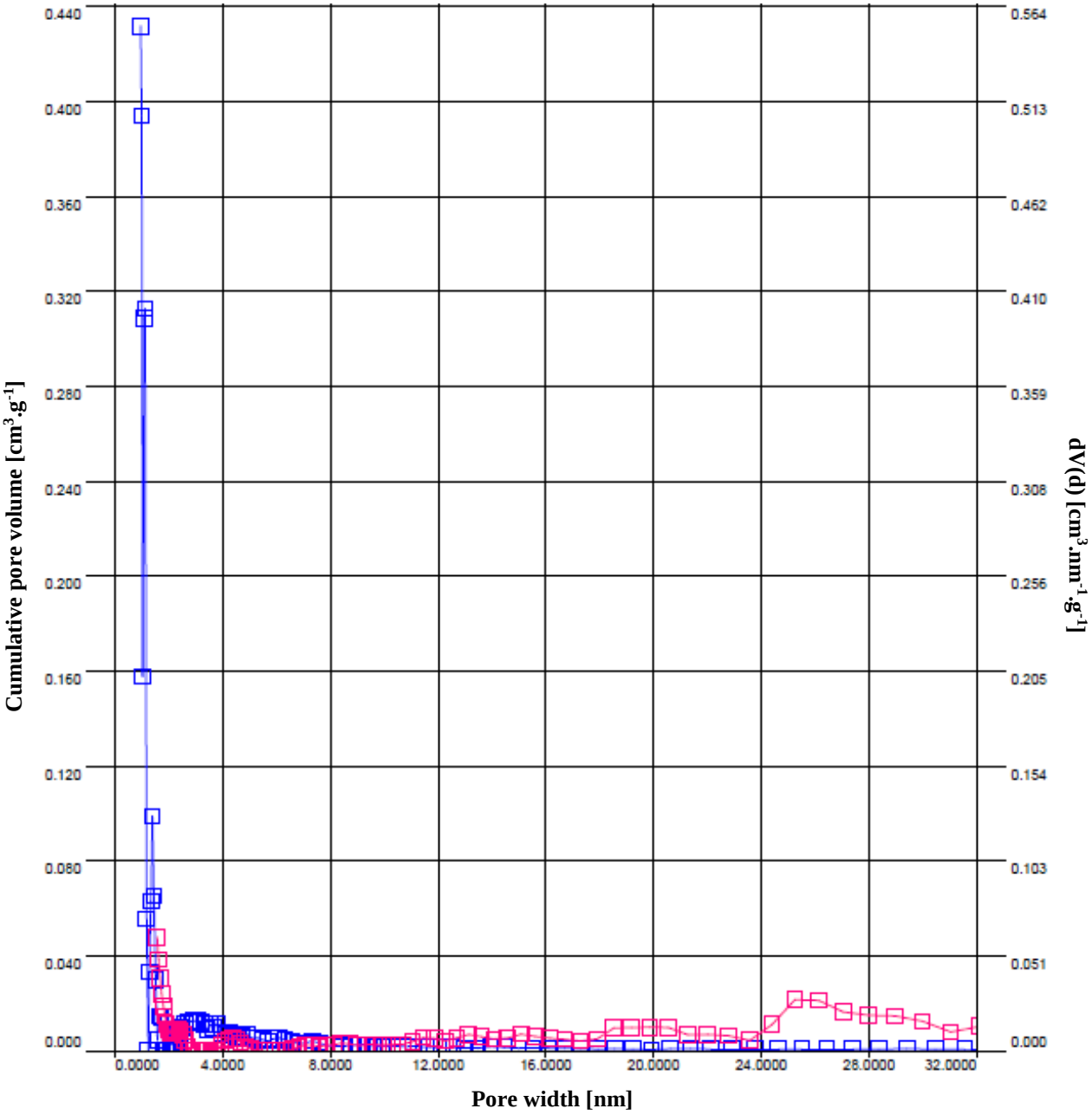

Fig. 27: The pore size distribution of JAK045A (pink) and JAK045B (blue) based on DFT.

4.4.2.2. Mesoporous Carbon Material (JAK040)

Similarly to the previous case, the resulting structure of this material named JAK040 was not highly ordered. Both micropores and mesopores within a wide PSD range were present, as can be seen from SEM photographs in Fig. 28 and PSD plot in Fig. 29. In comparison to the aforementioned synthesised carbon materials, this one was extremely fluffy. Due to this feature, JAK040 was also chosen for further functionalisation.

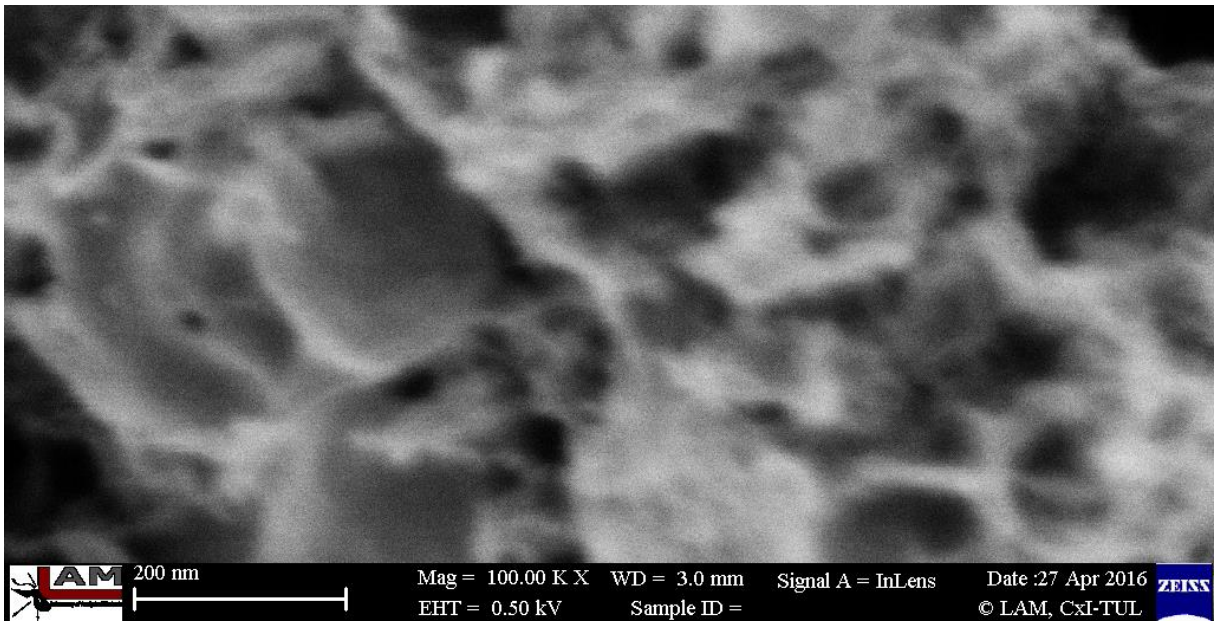

Fig. 28: SEM photograph of JAK040.

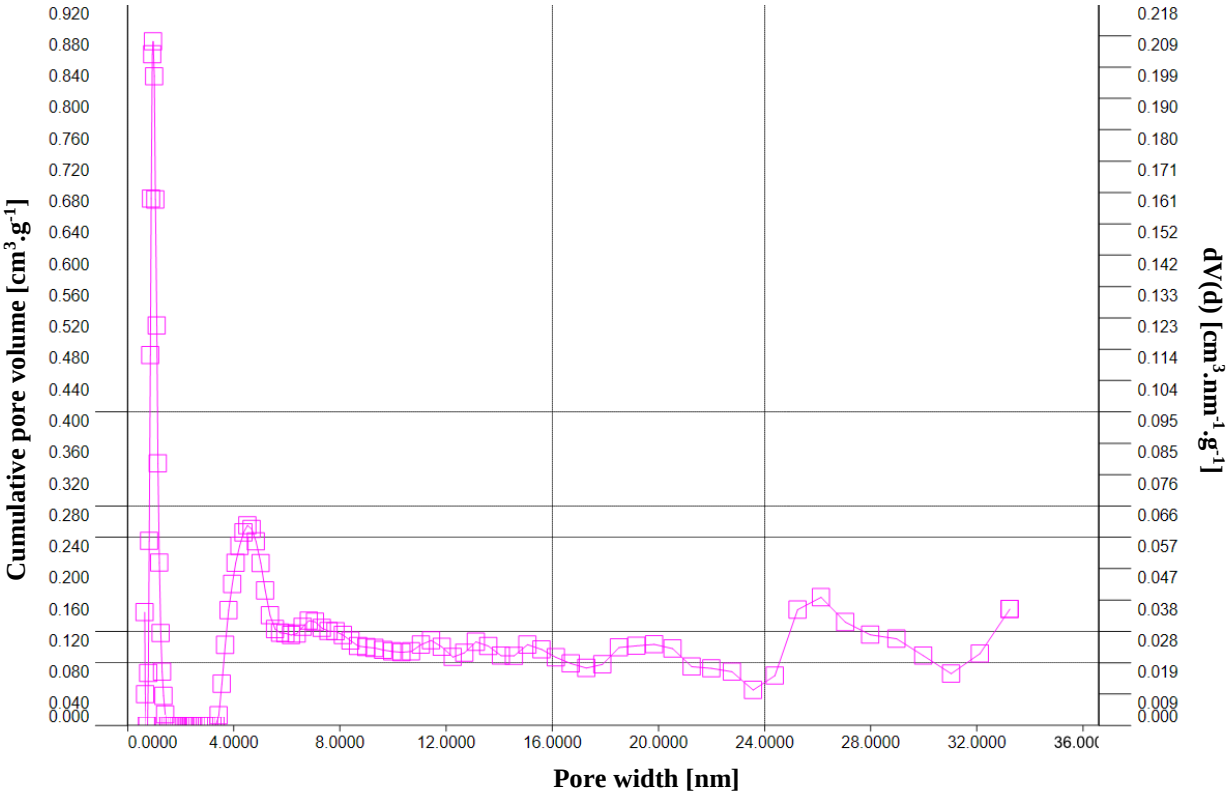

Fig. 29: The pore size distribution of JAK040.

In conclusion, hard-templated materials exhibited more ordered structures than the soft-templated ones. In addition, their preparation was reproducible, without any noticeable drawbacks. However, the procedures were lengthy, and dissolving the hard templates was an inconvenient step indeed, after which some residues of the templates may still have stayed blocked inside the porous structures.

4.4.3. Functionalised Materials

Three of the synthesised materials, namely JAK017B, JAK019 and JAK040, were functionalised with triethylenetetramine, and named JAK017B-TET, JAK019-TET and JAK040-TET.

Because of the fluffy structure of JAK040, the amount of the oxidising solution used was doubled in its case, in order to thoroughly soak the sample.

The results of the OEA in Tab. 9 show that the contents of nitrogen in JAK017B-TET and JAK019-TET were similar to that of commercially available CNPs Darco KB-G functionalised with TET (see Tab. 4 in chapter 4.1.3.). For JAK040-TET, the nitrogen content was lower, which may have been influenced by the sample's fluffy structure and slightly different oxidation conditions. In addition, more sulphur, which originated from the oxidation step, was found in this sample, despite a vigorous washing procedure.

	JAK017B-TET	**JAK019-TET**	**JAK040-TET**
Element		**OEA [wt. %]**	
C	76.98	62.27	82.08
N	5.31	4.58	2.25
S	2.39	2.56	5.58
H	3.06	1.2	2.13

Tab. 9: The results of OEA analysis of the synthesised materials functionalised with triethylenetetramine.

The X-ray fluorescence revealed that all samples contained traces of chlorine (from the chlorination step), which had not been substituted with triethylenetetramine, and JAK019-TET even some silicon, which could have been caused by blocking the silica precursor inside the carbon shells of JAK019. This would also help explain the lower content of carbon in this sample.

The results of surface area analyses are summarised in Tab. 10. All functionalised samples exhibited a significant decrease in their surface areas in comparison to the pristine synthesised materials.

Material	**Surface area [m^2 g^{-1}]**	**Material-TET**	**Surface area [m^2 g^{-1}]**
JAK017B	1927	JAK017B-TET	543.6
JAK019	155.1	JAK019-TET	64.6
JAK040	565.5	JAK040-TET	235.6

Tab. 10: Results of BET surface area analyses of the synthesised materials functionalised with triethylenetetramine.

Pore size distribution plots of the pristine and functionalised synthesised carbon materials are shown in Fig.30-32. While the pore volumes decreased noticeably because of the decrease in surface areas, the PSDs of the pristine synthesised carbon materials did not significantly differ from the functionalised. It can be therefore assumed that the surface was functionalised homogeneously. The best correlation of the PSD curves can be seen for JAK040 and JAK040-TET in Fig. 32.

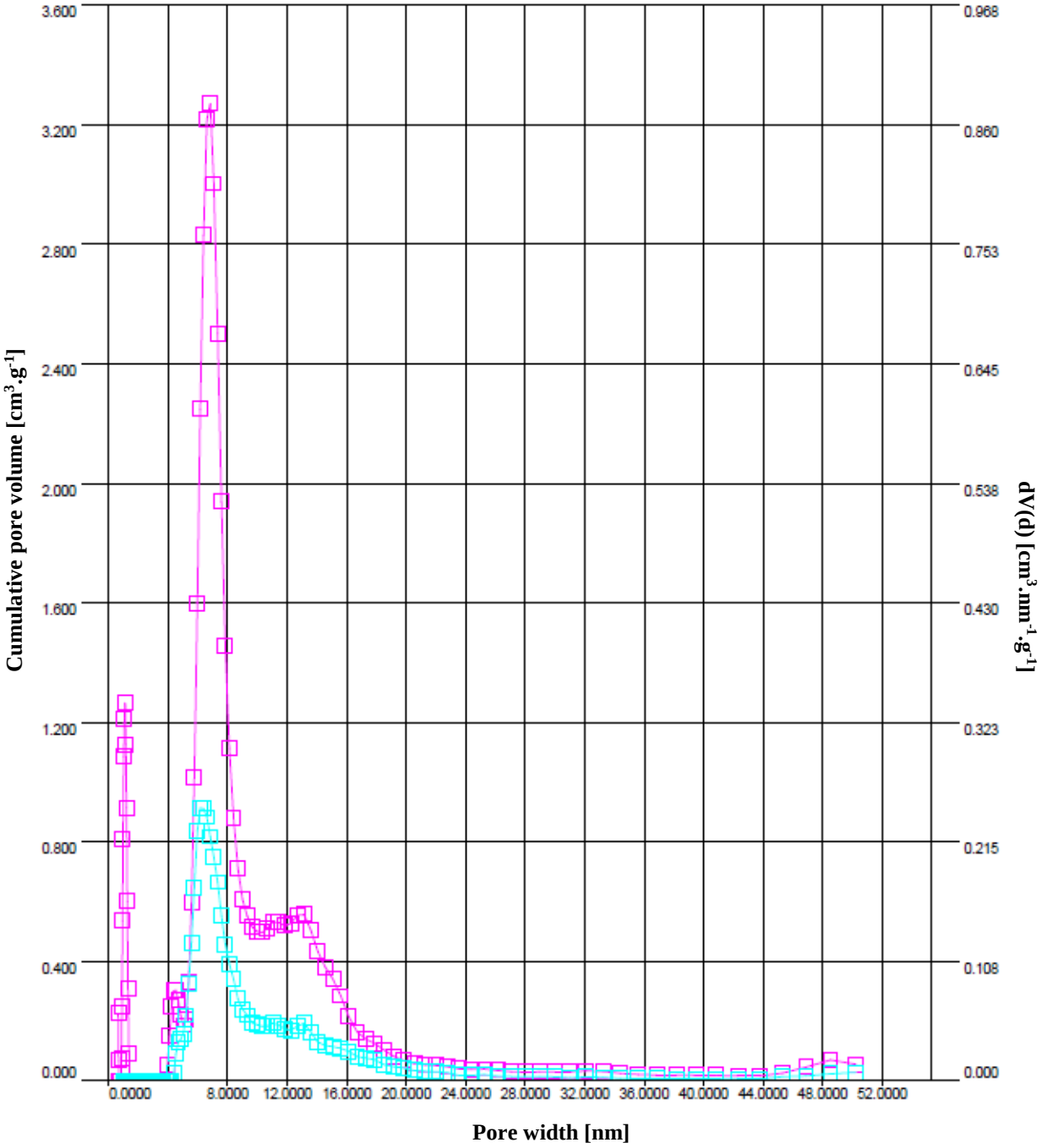

Fig. 30: The pore size distribution of JAK017B (pink) and JAK017B-TET (cyan) based on DFT.

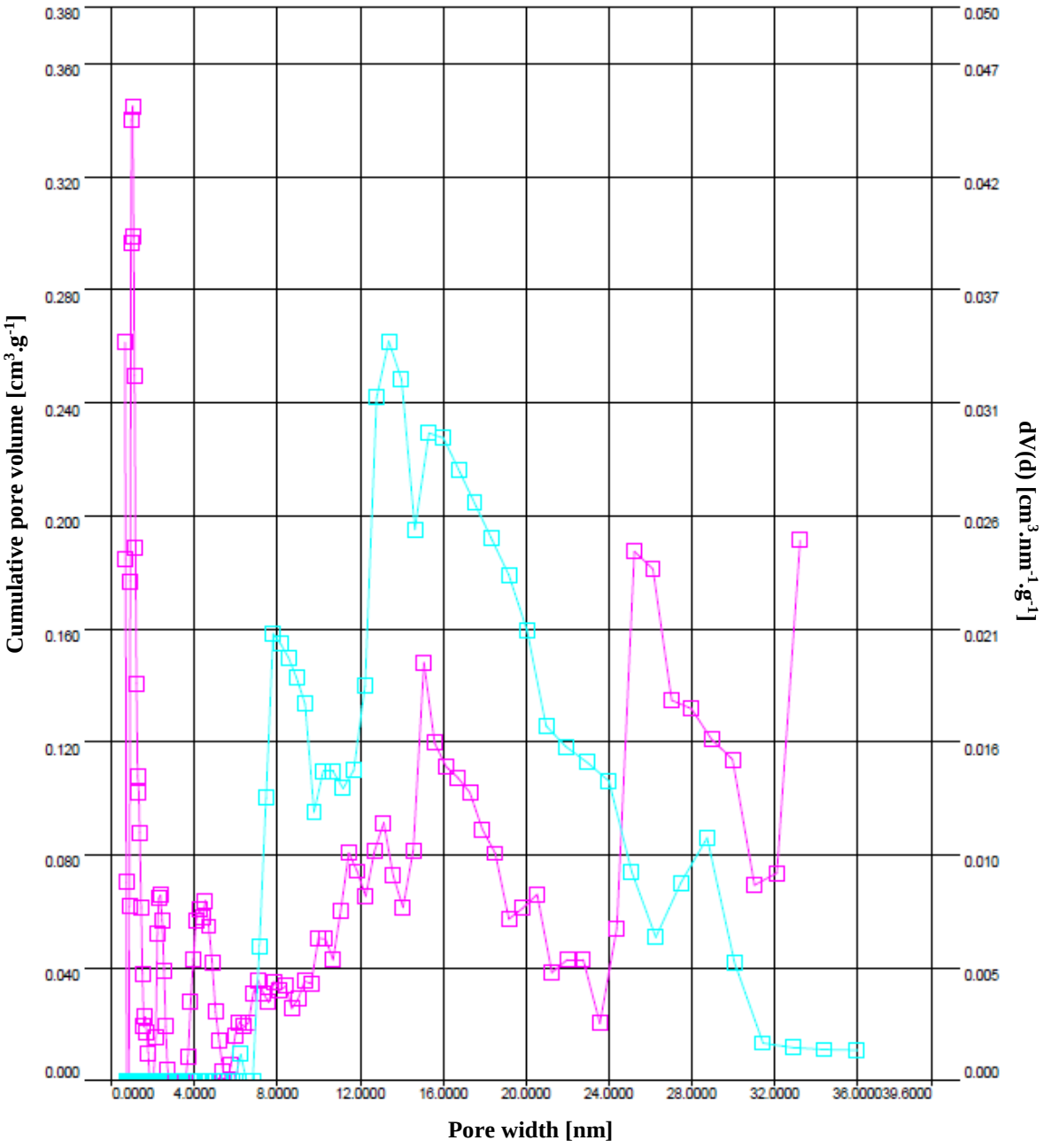

Fig. 31: The pore size distribution of JAK019 (pink) and JAK019-TET (cyan) based on DFT.

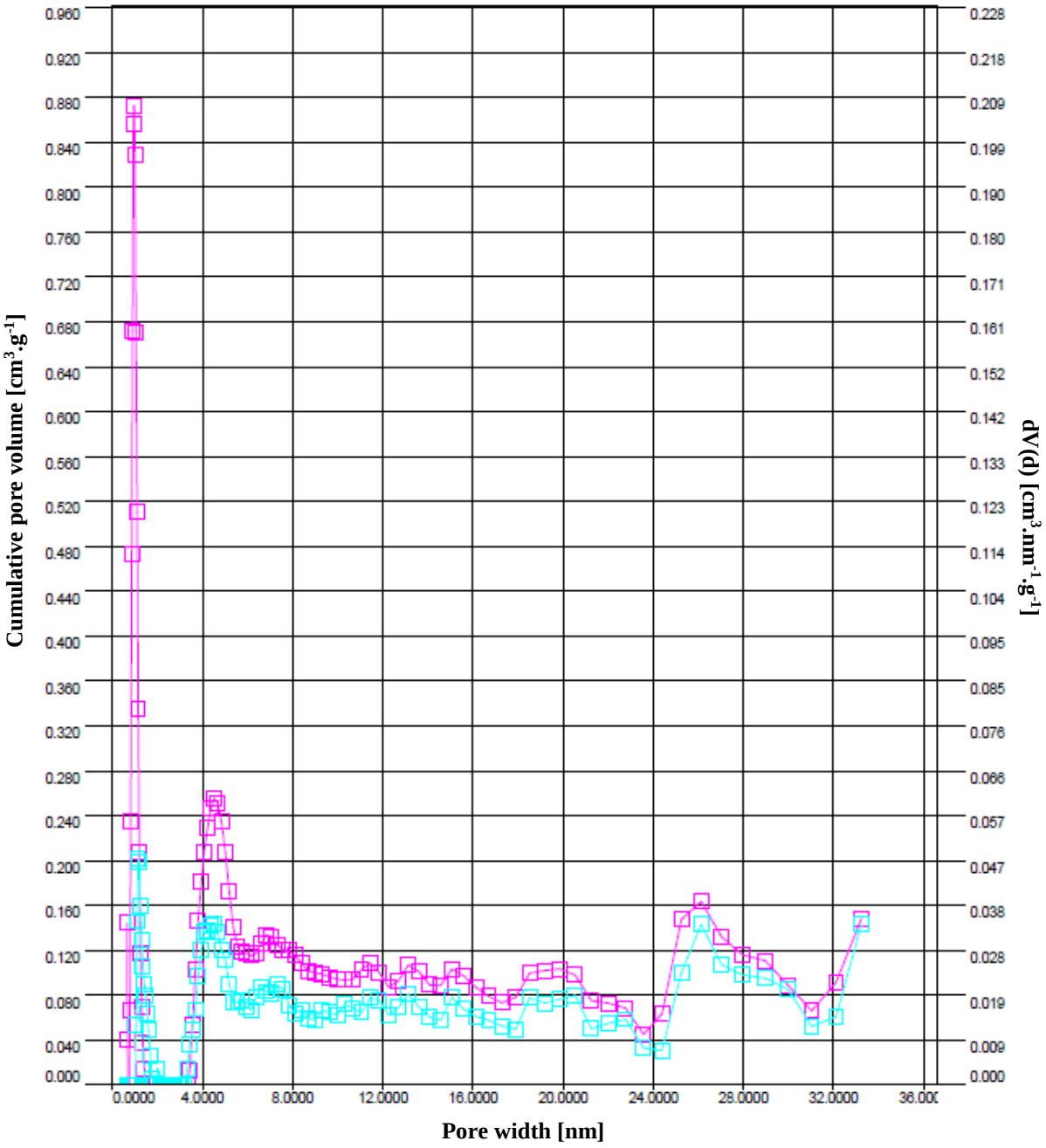

Fig. 32: The pore size distribution of JAK040 (pink) and JAK040-TET (cyan) based on DFT.

5. CONCLUSIONS

In the first part of this work, commercially available CNPs were successfully functionalised via a novel type of functionalisation, resulting in amide-amine groups on their surface. The oligoamines used varied in the length of alkyl chains and the number and type of amino groups. Although TEM images did not show any significant difference in the structure of the materials before and after functionalisation, the functionalisation modified the materials' properties to a large extent. The successful functionalisation was therefore confirmed via several analytical methods.

The wettability of the surfaces increased noticeably, and so did zeta potential. The results of XPS and OEA showed that nitrogen was present on the surface of the functionalised CNPs. The amount of nitrogen on the surface of the CNPs seemed to be influenced by the structure of the oligoamines (as more branched, secondary and tertiary amino groups containing oligoamines would not bind as easily as primary, less branched amines). The surface area and pore volume decreased distinctively after functionalisation, suggesting that pores were filled with bonded oligoamines.

Functionalised CNPs were grafted on plasma treated PET and HDPE. The polymer samples in subsequent stages of modification were characterised by various diagnostic methods. After the interaction of Ar plasma activated polymer surfaces with functionalised CNPs, an increase in nitrogen concentration on the very surface was observed. XPS, Raman spectroscopy, contact angle measurements and electrokinetic analysis confirmed that the functionalised CNPs were chemically bonded on the surface of the plasma treated polymers. Functionalised CNPs grafting on the plasma activated polymers had a positive effect on VSMCs adhesion and proliferation tested *in vitro*. The viability of cells cultivated on all grafted types of functionalised CPs was extremely high; except for the 1st day, on which the cells were still adapting to modified surface, the cell viability was above 95 %. However, differences in the numbers of cultivated cells among the individual types of the grafted CNPs were insignificant (Žáková et al., 2016). It can be therefore assumed that the structure of the amino chains did not play an important role in cell adhesion.

The aforementioned functionalised CNPs were also used to prepare composite scaffolds via sputtering the CNPs into electrospun polycaprolactone (PCL) nanofibers: three of them with three types of functionalised CNPs and one with plain activated CNPs. Plain PCL nanofibers and the composite nanofibrous scaffold with plain activated CNPs were used as comparative samples. The structure of the materials was studied using scanning electron microscopy (SEM), which showed that the materials containing the CNPs consisted of both micro- and nanofibres, while pristine PCL samples were nanofibrous. In comparison to pristine PCL nanofibers, the specific surface area of the scaffolds containing the CNPs significantly increased.

Cytocompatibility of the materials was tested using 3T3 mouse fibroblasts. Cell viability and proliferation was measured by MTT assay on days 1, 3, 8 and 14 after cell seeding. The samples were then stained using fluorescent dyes and examined via fluorescence microscopy. During the FM analyses, all scaffolds containing CNPs underwent structural thermal degradation when irradiated with either green or blue light. No damage was caused using UV light, which is in accordance with the fact that carbon materials, especially carbon black, are widely used as UV stabilisers in polymer production. The scaffolds with functionalised CNPs showed better cytocompatibility than the scaffold with plain CNPs. Nevertheless, the performance of pristine PCL fibres was still even better than that of the scaffolds containing the functionalised CNPs.

In conclusion, functionalisation positively influenced the CNPs cytocompatibility, however, it would have been more useful to incorporate the functionalised CNPs into a material that is not as highly cytocompatible as PCL.

On the basis of the results of MTT testing, the PCL scaffold with pristine CNPs was also tested for antibacterial activity (in comparison with pristine PCL nanofibers) using the bacterial strains of *E. coli*, *S. aureus*, *P. aeruginosa* and *E. faecalis*. However, no antibacterial effect was found.

A substantial part of the thesis was also aimed at the synthesis of mesoporous carbon particles via soft- and hard-templating. Although there have been many experiments to prepare various materials, unexpected issues occurred during autoclaving and carbonisation, so there were only a few batches in relatively high yields that were sufficient for further functionalisation. The materials were analysed using SEM and gas adsorption analyses. Selected synthesised materials were functionalised using the above mentioned amide-amine functionalisation and characterised using OEA and gas adsorption. The results of the OEA confirmed a successful functionalisation, showing a distinctive increase in nitrogen concentration. In the case of one hard-templated sample, a noticeable amount of silicon was found, which may have been caused by the presence of the residues of the spherical hard template, encapsulated inside carbon shells. The surface area of the functionalised templated materials decreased, as it had happened in the case of functionalised commercially available CNPs. The pore size distribution changed only slightly, showing similar trends and suggesting mainly micropore filling.

The templated and functionalised materials have neither been used for grafting on plasma treated polymer surfaces nor tested for cytocompatibility yet. These steps are to be conducted in the future, so that we can observe the influence of not only functionalisation but also the nano-structures.

The author performed or actively participated in the majority of the procedures and analyses throughout the study, from synthesis and functionalisation, production of fibrous materials, plasma treatment, gas physisorption, to MTT/cytocompatibility/antibacterial testing (excluding testing mentioned in (Švorčík et al., 2014; Žáková et al., 2016)) and scanning electron and fluorescence microscopy.

6. ABBREVIATIONS

AFM	Atomic force microscopy
ARXPS	Angle resolved X-ray photoelectron spectroscopy
BET	Brunauer-Emmet-Teller
BJH	Barrett-Joyner-Halenda
BSA	Bovine serum albumin
CA	Contact angle
CFU	Colony forming unit
DAPI	4',6-diamidino-2-phenylindole
DFT	Density functional theory
DMEM	Dulbecco's modified Eagle's medium
ECM	Extra cellular matrix
E. coli	*Escherichia coli*

E. faecalis	*Enterococcus faecalis*
FTIR	Fourier-transform infrared
FBS	Fetal bovine serum
FM	Fluorescent microscopy
FT-NIR	Fourier transform near-infrared
HDPE	High density polyethylene
HMDA	Hexamethylenediamine
IPA	Isopropyl alcohol
MRI	Magnetic resonance imaging
MTT	(3-(4,5-dimethylthiazol-2-yl)-2,5-diphenyltetrazolium bromide
NIR SERS	Near-infrared excited surface-enhanced Raman scattering
NPs	Nanoparticles
OD	Optical density
OEA	Organic elemental analysis
OMC	Ordered mesoporous carbon
P123	Pluronic 123
PBS	Phosphate buffered saline
PEG	Poly ethylene glycol
PET	Polyethylene terephtalate
PI	Propidium iodide
PSD	Pore size distribution
P. aeruginosa	*Pseudomonas aeruginosa*
RT	Room temperature
SBA-15	Santa Barbara amorphous
SEM	Scanning electron microscopy
STP	Standard temperature and pressure
SWCNTs	Single-walled carbon nanotubes
S. aureus	*Staphylococcus aureus*
TEM	Transmission electron microscopy
VSMC	Vascular smooth muscle cell
XPS	X-ray photoelectron spectroscopy

7. REFERENCES

Bacakova, L.; Filova, E.; Kubies, D.; Machova, L.; Proks, V.; Malinova, V.; Lisa, V.; Rypacek, F. Adhesion and Growth of Vascular Smooth Muscle Cells in Cultures on Bioactive RGD Peptide-Carrying Polylactides. *J. Mater. Sci.-Mater. Med.* **2007**, *18* (7), 1317–1323.

Bacakova, L.; Filova, E.; Parizek, M.; Ruml, T.; Svorcik, V. Modulation of Cell Adhesion, Proliferation and Differentiation on Materials Designed for Body Implants. *Biotechnol. Adv.* **2011**, *29* (6), 739–767.

Enyashin, A. N.; Ivanovskii, A. L. Structural and Electronic Properties of New 1D and 2D Carbon Allotropes with Mixed sp1 − sp3 Hybridization Types. *Chem. Phys. Lett.* **2014**, *609*, 15–20.

Falcao, E. H.; Wudl, F. Carbon Allotropes: Beyond Graphite and Diamond. *J. Chem. Technol. Biotechnol.* **2007**, *82* (6), 524–531.

Figueiredo, J. L.; Pereira, M. F. R.; Freitas, M. M. A.; Orfao, J. J. M. Modification of the Surface Chemistry of Activated Carbons. *Carbon* **1999**, *37* (9), 1379–1389.

Gómez-Serrano, V.; Acedo-Ramos, M.; López-Peinado, A. J.; Valenzuela-Calahorro, C. Oxidation of Activated Carbon by Hydrogen Peroxide. Study of Surface Functional Groups by FT-I.r. *Fuel* **1994**, *73* (3), 387–395.

Guedidi, H.; Reinert, L.; Lévêque, J.-M.; Soneda, Y.; Bellakhal, N.; Duclaux, L. The Effects of the Surface Oxidation of Activated Carbon, the Solution pH and the Temperature on Adsorption of Ibuprofen. *Carbon* **2013**, *54*, 432–443.
Haydar, S.; Ferro-García, M. .; Rivera-Utrilla, J.; Joly, J. . Adsorption of P-Nitrophenol on an Activated Carbon with Different Oxidations. *Carbon* **2003**, *41* (3), 387–395.
Hirsch, A. The Era of Carbon Allotropes. *Nat. Mater.* **2010**, *9* (11), 868–871.
Inagaki, M.; Kang, F.; Toyoda, M.; Konno, H. Chapter 1 - Introduction. In *Advanced Materials Science and Engineering of Carbon*; Inagaki, M., Kang, F., Toyoda, M., Konno, H., Eds.; Butterworth-Heinemann: Boston, 2014; pp 1–13.
Jaramillo, J.; Álvarez, P. M.; Gómez-Serrano, V. Oxidation of Activated Carbon by Dry and Wet Methods: Surface Chemistry and Textural Modifications. *Fuel Process. Technol.* **2010**, *91* (11), 1768–1775.
Lemus-Yegres, L. J.; Such-Basáñez, I.; Román-Martínez, M. C.; de Lecea, C. S.-M. Catalytic Properties of a Rh–diamine Complex Anchored on Activated Carbon: Effect of Different Surface Oxygen Groups. *Appl. Catal. Gen.* **2007**, *331*, 26–33.
Li, Y.; Zhong, J.; Yang, X.; Lan, G.; Tang, H.; Liu, H. Simple Synthesis of Semi-Graphitized Ordered Mesoporous Carbons with Tunable Pore Sizes. *New Carbon Mater.* **2011**, *26* (2), 123–129.
Lowell, S.; Shields, J. E.; Thomas, M. A.; Thommes, M. *Characterization of Porous Solids and Powders: Surface Area, Pore Size and Density*; Springer Science & Business Media, 2012.
Padil, V. V. T.; Nguyen, N. H. A.; Ševců, A.; Černík, M. Fabrication, Characterization, and Antibacterial Properties of Electrospun Membrane Composed of Gum Karaya, Polyvinyl Alcohol, and Silver Nanoparticles. *J. Nanomater.* **2015**, *2015*.
Reznickova, A.; Kolska, Z.; Siegel, J.; Svorcik, V. Grafting of Gold Nanoparticles and Nanorods on Plasma-Treated Polymers by Thiols. *J. Mater. Sci.* **2012**, *47* (17), 6297–6304.
Silva, W. M.; Ribeiro, H.; Seara, L. M.; Calado, H. D. R.; Ferlauto, A. S.; Paniago, R. M.; Leite, C. F.; Silva, G. G. Surface Properties of Oxidized and Aminated Multi-Walled Carbon Nanotubes. *J. Braz. Chem. Soc.* **2012**, *23* (6), 1078–+.
Švorčík, V.; Makajová, Z.; Slepičková Kasálková, N.; Kolská, Z.; Žáková, P.; Karpíšková, J.; Stibor, I.; Slepička, P. Cytocompatibility of Polymers Grafted by Activated Carbon Nano-Particles. *Carbon* **2014**, *69*, 361–371.
Thommes, M.; Kaneko, K.; Neimark, A. V.; Olivier, J. P.; Rodriguez-Reinoso, F.; Rouquerol, J.; Sing, K. S. W. Physisorption of Gases, with Special Reference to the Evaluation of Surface Area and Pore Size Distribution (IUPAC Technical Report). *Pure Appl. Chem.* **2015**, *87* (9–10).
Trostová, S.; Stibor, I.; Karpíšková, J.; Kolská, Z.; Švorčík, V. Characterization of Surface Chemical Modified Carbon Nano-Particles. *Mater. Lett.* **2013**, *102–103*, 83–86.
Žáková, P.; Slepičková Kasálková, N.; Kolská, Z.; Leitner, J.; Karpíšková, J.; Stibor, I.; Slepička, P.; Švorčík, V. Cytocompatibility of Amine Functionalized Carbon Nanoparticles Grafted on Polyethylene. *Mater. Sci. Eng. C* **2016**, *60*, 394–401.

8. LIST OF PUBLICATIONS

h-index: 3
Oral presentations at international conferences (abroad): 5 (4)
Poster presentations at international conferences (abroad): 4 (2)

8.1. Articles in impacted journals

a) Žáková, P., Slepičková Kasálková, N., Kolská, Z., Leitner, J., Karpíšková, J., Stibor, I., Slepička, P., Švorčík, V: Cytocompatibility of Amine Functionalized Carbon Nanoparticles Grafted on Polyethylene. *Materials Science and Engineering: C* 60 (1 March 2016): 394–401. doi:10.1016/j.msec.2015.11.058.

b) Švorčík, V., Makajová, Z., Slepičková Kasálková, N., Kolská, Z., Žáková, P., Karpíšková, J., Stibor, I., Slepička, P.: Cytocompatibility of Polymers Grafted by Activated Carbon Nano-Particles. *Carbon* 69 (April 2014): 361–71. doi:10.1016/j.carbon.2013.12.037.

c) Trostová, S., Stibor, I., Karpíšková, J., Kolská, Z., Švorčík, V.: Characterization of surface chemical modified carbon nano-particles, *Materials Letters*, Volumes 102–103, July 2013, 83-86. doi:10.1016/j.matlet.2013.03.119.

d) Šlamborová, I., Zajícová, V.,Karpíšková, J., Exnar, P., Stibor, I.; New type of protective hybrid and nanocomposite hybrid coatings containing silver and copper with an excellent antibacterial effect especially against MRSA, *Materials Science and Engineering: C*, Volume 33, Issue 1, 1 January 2013, 265-273, ISSN 0928-4931. doi: 10.1016/j.msec.2012.08.039

8.2. Articles in non-impacted journals

a) Šlamborová, I., Zajícová, V., Karpíšková, J. a Exnar, P.: Immobilisation of antibiotic tetracycline on silica nanofibres. *Vlákna a Textil*. 2012, 19(2), 3-9. ISSN 1335-0617.

8.3. Conferences

- oral presentations:

a) Karpiskova, J., Pilarova, K., Jencova, V., Stibor, I., Chvojka, J., Mikes, P., Nguyen, H. A. N.: Cytocompatibility of Polycaprolactone Nano-Microfibrous Scaffolds Loaded with Amide-Amine Functionalised Carbon Nanoparticles, *6th EuCheMS 2016 Chemistry Congress, Seville, Spain*. September 11-15 2016

b) Karpiskova, J., Pilarova, K., Jencova, V., Stibor, I., Chvojka, J., Mikes, P., Nguyen, H. A. N.: Cytocompatibility of Polycaprolactone Nano-Microfibrous Scaffolds Loaded with Amide-Amine Functionalised Carbon Nanoparticles, *NANOinBIO 2016: Advances for life & Materials Science, Guadeloupe*. May-June 2016.

c) Karpiskova, J., Pilarova, K., Jencova, V., Stibor, I., Chvojka, J., Mikes, P.: Polycaprolactone Nanofibrous Scaffolds Loaded with Amide-Amine Functionalised Carbon Nanoparticles and Their Effect on 3T3 Mouse Fibroblasts. *International Conference on Nanoscience, Nanotechnology and Advanced Materials NANOS15, Visakhapatnam, India.* December 2015

d) Karpiskova, J., Pilarova, K., Jencova, V., Stibor, I., Chvojka, J., Mikes, P.: Polycaprolactone Micro-Nanofibrous Scaffolds Loaded with Amide-Amine Functionalised Carbon Particles and Their Effect on 3T3 Mouse Fibroblasts. *NANOCON 2015, 7th International Conference, Brno*, 14-16 October 2015

e) Karpiskova, J., Pilarova, K., Jencova, V., Stibor, I., Chvojka, J., Mikes, P.: Polycaprolactone Nanofibrous Scaffolds Loaded with Amide-Amine Functionalised Carbon Nanoparticles and Their Effect on 3T3 Mouse Fibroblasts. *2nd Annual International Conference on Nanoscience and Nanotechnology (ICNSNT) 2015, Colombo, Sri Lanka*. September 2015

-posters and other:

a) Žáková, P., Slepičková Kasálková, N., Slepička, P., Švorčík, V.: Cell adhesion and proliferation on amine functionalized carbon nanoparticles grafted biopolymer. *NANOCON 2015, 7th International Conference, Brno,* 14-16 October 2015–article in conference proceedings and poster

b) Karpíšková, J., Stibor, I., Švorčík, V., Makajová, Z., Slepičková Kasálková, N., Kolská, Z., Žáková, P., Slepička, P.: Polymer Surfaces Grafted With Functionalized Carbon Nanoparticles For Cell Culturing. *5th EuCheMS Chemistry Congress, Istanbul, Turkey,* 31 August-4 September 2014 – poster

c) Karpíšková, J., Stibor, I., Švorčík, V., Makajová, Z., Slepičková Kasálková, N., Kolská, Z., Žáková, P., Slepička, P.: Cytocompatibility Of Polymer Surfaces Grafted With Amid-Amine Functionalized Carbon Nanoparticles, *Challenges in Nanoscience ISACS 15, San Diego, California*, 17-20 August 2014 – poster

d) Karpíšková, J., Stibor, I., Švorčík, V., Makajová, Z., Slepičková Kasálková, N., Kolská, Z., Žáková, P., Slepička, P.: Surfaces with Carbon Nanoparticles for Medical Applications, 5th *International Conference Nanocon, Brno*, 16-18 October 2013 –article in conference proceedings and poster

e) Švorčík, V., Makajova, Z., Slepičková Kasálková, N., Kolská, Z., Stibor, I., Karpíšková, J., Žáková, P., Slepička, P.: Cytocompatibility of polymers grafted by activated carbon nano-particles, *XVII Eur. Conf. Anal. Chem., Warsaw, Poland,* 25-29 August 2013 – poster

f) Šlamborová, I., Zajícová, V., Stibor, I., Karpíšková, J., Exnar, P.: High Protective Hybrid Coating Containing Silver, Copper and Zinc Ions with an Excellent Antibacterial Effect Especially Against Bacterial Strains of MRSA. *Potential and Application of Nanotreatment of Medical Surfaces – Book of Extended Abstracts Liberec* – TUL2012, 4, ISBN: 978-80-7372-890-8. – article in conference proceedings

g) Karpíšková, J.: Antibiotické látky ve vybraných rostlinách. *Jelenia Gora: 5th International Conference of Young Scientists, 2011*. ISBN 978-83-62708-21-5 – 1st award winning article in conference proceedings

h) Karpíšková, J.: Zkoumání antibiotických látek v rostlinách. *Sborník přednášek z mezinárodní konference Trojanovice.* September 29 – October 1 2010. Přírodovědecká Fakulta Ostravské univerzity v Ostravě, edit.: A. Chupáč, J. Vermířovský. ISBN 978-80-7368-426-6. – article in conference proceedings

i) Grégr, J., Karpíšková, J., Kopecká, V., Slavík, M.: ICT pro řešení problémů chemie rostlinných látek, *Aktuální trendy ICT ve výuce chemie – Current trends of ICT in chemistry education XX, Book of abstracts,* p. 47, ISBN 978-80-7041-082-5.

j) Grégr, J., Karpíšková, J., Kopecká, V., Slavík, M ., Šlamborová, I.: ICT pro řešení problémů chemie rostlinných látek – ICT for Solving Problems of Herbal Chemistry, *Media4u Magazine X3/2010*, str. 186, ISSN 1214-9187.

k) Jodas, B., Grégr, J., Karpíšková, J., Slavík, M.: Problémové úlohy v chemii řešené pomocí molekulární vizualizace, *Sborník přednášek 19. mezinárodní konference o výuce chemie*, 2. část: Přehledové studie a krátké informace, Hradec Králové, IX-2009, edit.: M. Bílek, str. 247-250, ISBN 978-80-7041-839-0.